





## A Probabilistic Cut Finite Element Method With Random Field Generator and Bayesian Model Calibration for Flow Through Rough Cracks

Brubeck Lee Freeman<sup>1,2</sup> Evan John Ricketts<sup>2</sup> Diane Gardner<sup>2</sup> Anthony Jefferson<sup>2</sup> Peter John Cleall<sup>2</sup> Pierre Kerfriden<sup>3</sup>

<sup>1</sup>LUSAS, Kingston upon Thames, Surrey, UK | <sup>2</sup>Cardiff University, Cardiff, UK | <sup>3</sup>Centre De Matériaux, Mines Paris/PSL University, Evry, France

Correspondence: Brubeck Lee Freeman (brubeck.freeman@lusas.com; freemanbl@cardiff.ac.uk) | Evan John Ricketts (RickettsE1@cardiff.ac.uk)

Received: 6 November 2024 | Revised: 19 September 2025 | Accepted: 3 October 2025

Funding: This study was funded by the EPSRC Grant EP/P02081X/1, 'Resilient Materials for Life (RM4L)' and Finite Element Company LUSAS (www.lusas.com).

Keywords: Bayesian model calibration | cut finite element method | fluid flow | probabilistic finite element method | random field | rough cracks

#### **ABSTRACT**

A new model for the simulation of fluid flow through rough cracks is presented. The model combines a probabilistic cut finite element method (PCutFEM) to capture the unfitted boundary condition at the fluid interface, with a stochastic random field generator to represent the crack asperities. A key feature of the model is the consideration of the crack roughness and tortuosity, which are calculated from the crack asperities. This approach avoids the need for empirical reduction factors, whilst allowing for the heterogeneity of the flow processes. In addition to this, the model considers the spatially varying crack width associated with material loss during the fracture process, which is represented using a smoothed Gaussian noise. To determine the statistical parameters that describe the crack asperities, a Bayesian statistical inference is employed. The statistical inference considers the uncertainty in measured values, observations of crack permeabilities and the stochastic nature of the random field model. The performance of the model is assessed via comparison with new experimental data of the flow of tap water (TW) and a ground-granulated blast furnace slag (GGBS) suspension through concrete cracks. In addition, a statistical analysis is employed to quantify the level of uncertainty in the predictions. The results of the validation show that the model is able to accurately reproduce the observed experimental behaviour and that a confidence level in the results of 95% is achieved in eight simulations.

### 1 | Introduction

Understanding fluid flow behaviour through cracks is of key importance for a range of applications, including (but not limited to) underground energy storage and utilisation [1, 2], geological sequestration of  $CO_2$  [3, 4] and construction [5–7]. For example, consideration of fluid flow through fractures is vital in the design of some concrete structures. The presence of concrete cracks exacerbates durability issues such as the corrosion of steel reinforcement [7] and carbonation [5] due to increased rates of

ingress of moisture and deleterious chemical species such as chlorides. One approach to mitigate such issues is to design the concrete to be self-healing, such that cracks are healed as they form [8]. Several self-healing techniques rely on an encapsulated healing agent that is transported to the damage site through the cementitious matrix and cracks [9, 10]. Thus, healing efficacy is linked to the fracture flow behaviour [11, 12].

The permeability of cracks is most frequently derived from Poiseuille's law, assuming smooth parallel plates [13]. Real

This is an open access article under the terms of the Creative Commons Attribution License, which permits use, distribution and reproduction in any medium, provided the original work is properly cited.

© 2025 The Author(s). International Journal for Numerical and Analytical Methods in Geomechanics published by John Wiley & Sons Ltd.

cracks, however, are rough and tortuous, and exhibit effective permeabilities that can be orders of magnitude lower than those predicted by Poiseuille's law. To account for this, empirical reduction factors, which can vary significantly and are not linked to the crack geometry, are often employed [13]. To improve the estimation of the permeability, a number of researchers instead modify the permeability term using crack roughness and tortuosity factors, both of which can be explicitly calculated from the crack geometry [13–15].

Crack geometry may be obtained either through direct measurement of physical samples, using, for example, laser profilometry, or through the generation of representative virtual or synthetic fractures. For the latter, a number of approaches have been taken [16]. Garcia and Stoll [17] employed an uncorrelated Gaussian distribution of random numbers, to which Gaussian smoothing was applied to obtain a correlated profile to represent rough surfaces. Brown [18] employed a Fourier space-based technique for the generation of synthetic fractures that accounted for fractal dimension, roughness and mismatch length scale. The mismatch length scale was later improved upon by Glover et al. [19] and Ogilvie et al. [20] who allowed for a smooth transition between completely correlated to uncorrelated fracture surfaces (in the approach of Brown [18], the transition could be viewed as a step function). Guiltinan et al. [16] presented a python library for generating synthetic fractures, pySimFrac, based on the SynFrac model presented in Ogilvie et al. [20]. To demonstrate the use of the generated fractures with a flow model, examples were presented in which pySimFrac was combined with open-source Lattice-Boltzmann method (LBM) based models (e.g., MP-LBM [21] and MF-LBM [22]). The results showed that the heterogeneity of the crack geometry has a significant effect on velocity and phase saturation profiles.

Spatial variability impacts many hydrological processes associated with fluid flow and should be accounted for in numerical models. One approach to achieve this uses random fields with the stochastic finite element method (SFEM) [23]. The SFEM extends the finite element method (FEM) to consider variability, whether it be in the initial conditions, problem geometry or material properties. Field generation techniques vary widely, including Karhunen-Loève's expansion and local averaging subdivision methods [24, 25]. The most common method, however, is through computationally expensive covariance matrix decomposition [26–28], which is unsuitable for large-scale problems [28]. An alternative approach is to generate Gaussian random fields through the solution of a stochastic PDE related to the Matérn autocorrelation function (ACF) [29], which is used in the present work to represent variations in crack asperities. In addition to the uncertainty associated with the stochastic nature of such random field models, the statistical parameters that describe the crack geometry also have an associated uncertainty. To calibrate the statistical parameters, as well as account for uncertainties in their values, a Bayesian model calibration can be employed [30]. Bayesian model calibration alleviates the issues associated with conventional, trial and error-based calibration, whilst considering the uncertainty associated with the model and observed data [30-32]. In addition, Bayesian approaches allow for quantification of the uncertainty in model parameters and results through credible intervals [30, 32]. For a complete description of the application of Bayesian calibration to numerical models, the interested reader is referred to Kennedy and O'Hagan [33].

Finite element models that consider uncertainty have been developed for a wide range of problems, including structural mechanics [34, 35], multi-scale modelling and homogenisation [36, 37] and transport through porous media [38, 39]. According to Stefanou [40], uncertainty is often incorporated into these models (usually termed stochastic or probabilistic FEMs, SFEM and PFEM, respectively) using either Monte Carlo simulation (MCS) [35], the perturbation method [34, 41] or the spectral SFEM (SSFEM) [42]. A key advantage of such approaches is the ability to quantify the probability of model outcomes, such as structural failure [23]. Figiel and Kamiński [35] used MCS to investigate the sensitivity of fatigue delamination of a twolayer composite to a number of uncertain model parameters. The authors employed correlation coefficients and probabilistic sensitivity measures to estimate both the sensitivity of model outputs to input parameters and the relative significance of each input variable. Uncertainty in the finite element discretisation error was considered by Poot et al. [43]. The authors followed a Bayesian approach that updates a Gaussian process prior with observations of a right-hand side vector from a finite element discretisation. Girolami et al. [44] proposed a statistical finite element method (statFEM) to incorporate observed data into finite element models. statFEM employs a Bayesian approach that accounts for uncertainty stemming from the PFEM, measurement noise and model misspecification.

A number of models for the simulation of flow through rough fractures have been employed, many of which are based on LBM [45, 46] or continuum-based approaches such as the FEM or finite volume method (FVM) [47, 48]. The simulation of two-phase flows within rough fractures requires consideration of fluid-fluid interface conditions. Continuum-based approaches account for this with interface capturing/tracking techniques such as the volume of fluid or level-set method [47, 48]. Chen et al. [48] investigated the role of viscous and capillary forces on the flow behaviour using a volume of fluid method combined with the Navier-Stokes equations. The model was able to obtain good qualitative agreement with experimental observations concerning the invasion morphologies at the crack scale. Dai et al. [47] used an FEM combined with the level-set method to investigate the effect of roughness and wettability on the two-phase flow (of water and crude oil) through rough fractures. The model assumed that the fluid properties smoothly varied across the interface, whilst the interfacial force was applied as a function of the levelset. For two-phase flow, the interfacial force is associated with a jump in fluid stress across the interface [49]. For single-phase flow within an unsaturated crack, the fluid interface is associated with an unfitted boundary when using an FEM with a fixed mesh (which may be preferable to avoid complex re-meshing associated with topological changes) [49]. Such discontinuities, or unfitted boundary conditions, are not easily represented using the standard FEM. To address this, unfitted finite element methods (UFEMs) such as the extended and cut-finite element methods (XFEM and CutFEM, respectively), that use enrichment functions or overlapping elements to capture discontinuities, may be employed. A key drawback of many UFEMs is the need

for non-standard integration schemes on elements intersected by discontinuities that complicate their implementation [50]. However, there are now several approaches to circumventing this issue whilst maintaining optimal convergence properties, among which are the 'CutFEM without cutting the mesh' [50], shifted boundary and shifted interface methods (SBM and SIM respectively) [51, 52] and the cut-cell method of Pande et al. [53].

In the present work, we employ a probabilistic cut finite element method (termed PCutFEM) approach for simulating the flow through rough cracks, with a stochastic PDE-based approach for the representation of crack asperities, from which tortuosity and roughness are calculated. The fluid interface is tracked using the level-set method. For the representation of the spatial variability of the crack width associated with material loss during the fracture process, we employ a smoothed Gaussian noise. Finally, the statistical parameters used to describe the crack asperities are calibrated using a Bayesian model calibration that accounts for uncertainty in the measured parameters, observations of crack permeability and the stochastic nature of the random field model. The validation of the model is shown through the consideration of an example problem. The example problem concerns the flow of tap water (TW) and a ground-granulated blast furnace slag (GGBS) suspension through concrete fractures, for which new experimental data are presented.

The layout for the remainder of the paper is as follows; the theoretical formulation for the fluid flow, random field generation and Bayesian model calibration is presented in Section 2. Section 3 presents the numerical implementation. Section 4 presents a verification and validation example concerning the generation of virtual rough fractures and calculation of roughness, tortuosity and permeability. A validation example using new experimental data that concerns flow through concrete fractures is presented in Section 5 before some concluding remarks are given in Section 6.

## 2 | Theoretical Formulation

In the present work, we consider a stochastic random field model for the generation of virtual cracks, the parameters for which are calibrated using a Bayesian approach that uses experimental measurements of crack asperity correlation lengths and standard deviation, and crack permeabilities. The generated cracks are used to determine crack roughness and tortuosity values, which are fed into a PCutFEM model to simulate the fluid flow behaviour. Uncertainty in crack parameters, measured permeabilities and the stochastic nature of the random field model are all accounted for, and the resulting uncertainty is quantified through statistical analysis. An overview of the approach of the model that illustrates how the various components fit together is given in Figure 1.

It is noted that in the present work the focus is on simulating fluid flow solely within rough cracks. For flow through fractured porous media, the transport of fluids through the porous medium, as well as the transfer of fluids between the two domains would need to be considered (see e.g. [54–58]).

#### 2.1 | Fluid Flow

### 2.1.1 | Governing Equations

We consider two-phase flow of fluids through rough cracks and assume that one of the phases is air. In addition, we assume that the air pressure within the crack remains constant at atmospheric pressure (following the approach of [12, 54]), and that there is a sharp interface between the fluid and air phases. Therefore, it is assumed that within the crack domain there are discrete phases of fluid (fully saturated) and air, and never a mixture of these two phases. Under these assumptions, the two-phase crack flow is governed by the single fluid mass balance equation (i.e., the flow of air may be neglected), which, combined with Darcy's law for describing the fluid flux and the pressure boundary condition at the fluid interface, reads:

$$\frac{\partial \rho w}{\partial t} + \nabla \cdot (\rho w \mathbf{u}) = 0, \forall \mathbf{x} \in \Omega$$
 (1a)

$$\mathbf{u} = -K(\nabla P - \rho \mathbf{g}), \forall \mathbf{x} \in \Omega$$
 (1b)

$$P = P_d = P_c (1 - \beta_s) - 2 \frac{\beta_m}{\nu} \mathbf{u} \cdot \mathbf{n}, \forall \mathbf{x} \in \Gamma_f$$
 (1c)

in which  $\Omega$  is the problem/fluid domain (defined as the domain of the crack that is saturated with fluid),  $\Gamma_f$  is the fluid interface,  $\rho$  is the fluid density, w is the crack width,  $\mathbf{u}$  is the vector of fluid velocities, P is the fluid pressure,  $\mathbf{g}$  is the acceleration due to gravity,  $\mathbf{n}$  is the unit normal vector and  $\beta_s$  and  $\beta_m$  are factors accounting for stick-slip and frictional dissipation at the meniscus, respectively.

The crack permeability, K, is given as:

$$K = \frac{w^2}{\mu} + \frac{w\beta_w}{2} \tag{2}$$

in which  $\mu$  is the fluid viscosity and  $\beta_w$  is a wall slip factor.

The capillary pressure at the fluid interface is given by the Young–Laplace equation:

$$P_c(\theta_d) = \frac{2\gamma\cos(\theta_d)}{w} \tag{3}$$

where  $\gamma$  is the surface tension and  $\theta_d$  is the dynamic contact angle that is related to the static contact angle  $(\theta_s)$  via the relationship of Jiang et al. [59]:

$$\theta_d = a\cos(\cos(\theta_s) - \tan h(c_1 C a^{c_2})(\cos(\theta_s) + 1)) \tag{4}$$

where  $Ca = \mathbf{u} \cdot \mathbf{n}\mu/\gamma$  is the capillary number and  $c_1$  and  $c_2$  are constants.

#### 2.1.2 | Crack Tortuosity and Roughness

**2.1.2.1** | Calculation From Crack Asperities. Equation (2) for the crack permeability is valid only for smooth plates and does not account for the morphological characteristics of real cracks. To account for the reduction in permeability arising from the crack morphology, the crack permeability is often scaled by an

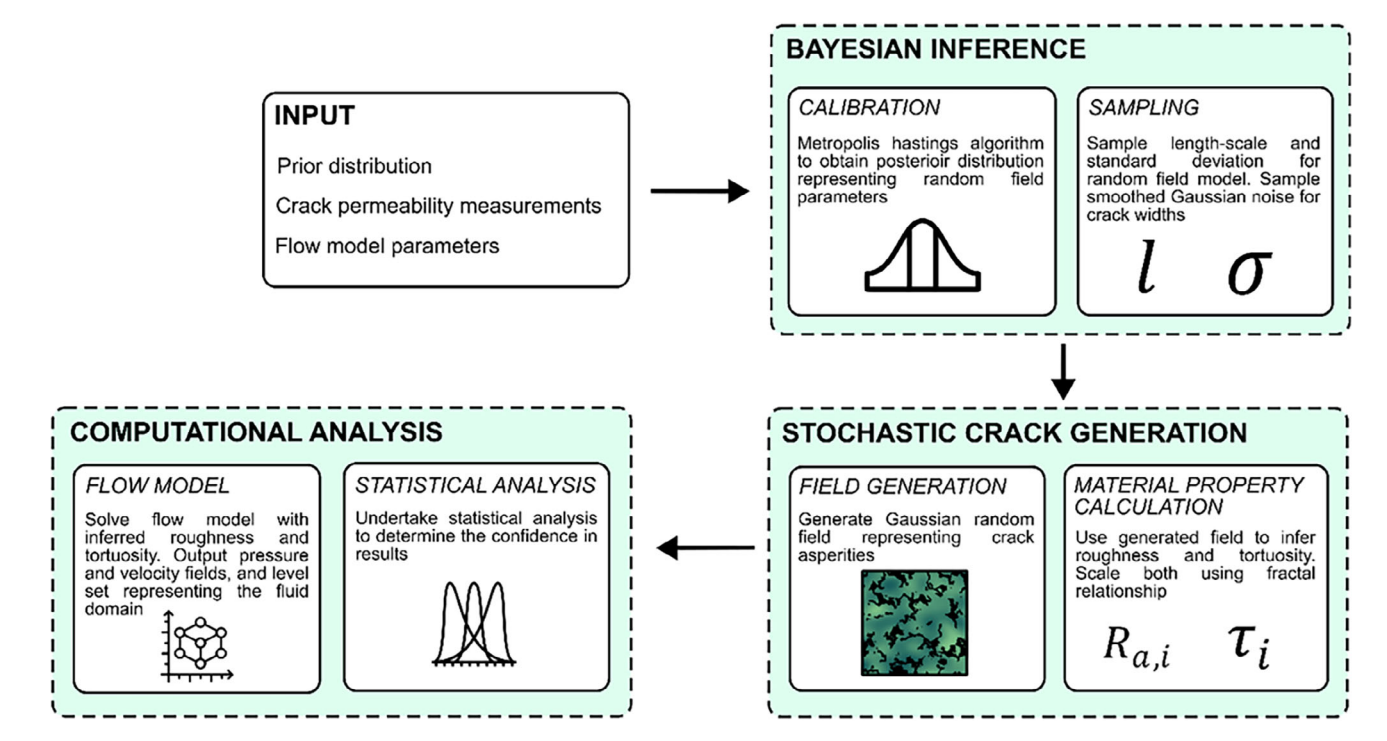


FIGURE 1 | Overview of model approach.

empirical reduction factor. However, as highlighted by Akhavan et al. [13], such values are often uncertain, can vary by orders of magnitude and are not correlated to the crack geometry.

A wide range of approaches have been taken to quantify morphological characteristics, such as magnitude, angularity and periodicity, of crack surfaces [60]. To this end, a number of roughness parameters have been defined [15]. The proposed roughness parameters include the joint roughness coefficient (JRC), mean asperity height ( $R_a$ ), surface roughness ( $R_s$ ), tortuosity ( $\tau$ ), rootmean-square of the first derivative of the profile ( $Z_2$ ) and the fractal dimension ( $D_f$ ), all of which have been incorporated in modifying the hydraulic conductivity of rough fractures [15].

Noting that a single roughness parameter may not be sufficient in quantifying the effect of the crack morphology on fluid flow [15, 60], the present work follows the approach of Akhavan et al. [13] and accounts for the effects of the crack morphology through both the mean asperity height (crack roughness) and crack tortuosity. Roughness and tortuosity are accounted for independently and are calculated directly from the crack geometry, where the latter is obtained from a random field generator used to represent the crack asperities.

Crack tortuosity is related to the deviation of the crack profile from a straight-line path, due to the crack asperities, leading to an effective crack length,  $L_e$ , and therefore flow path, that is larger than the nominal crack length,  $L_{\rm nom}$  [13]. The crack tortuosity is defined as the ratio:

$$\tau = \left(\frac{L_{\text{nom}}}{L_e}\right)^2 \tag{5}$$

In the present work, the crack roughness is defined as the mean height of the crack asperities with respect to a reference line. The reference line is obtained by dividing the crack profile into segments of length,  $L_{\rm seg}$ , and connecting the beginning and end points where the segment intersects the crack profile [13]. The height of a crack asperity with respect to the reference line is defined as:

$$R_a = \|Z_{\rm asp} - Z_{\rm ref}\| \tag{6}$$

where  $Z_{\text{asp}}$  and  $Z_{\text{ref}}$  are the height of the surface asperity and reference line respectively and  $\|\cdot\|$  denotes the Euclidean distance.

An illustration of these concepts can be seen in Figure 2.

The calculation of crack roughness and tortuosity is described in the following: the first step is to discretise the crack into a mesh comprising ne elements of length h, and nd nodes. Once the discretisation is established, the crack asperity height is obtained either from an image, if using experimental data, or from the random field generator.

Following this, the crack tortuosity ( $\tau$ ) can be calculated for each node as follows:

$$\tau_{i} = \frac{1}{nj} \sum_{j=1}^{nj} \left( \frac{h}{L_{e}} \right)^{2} = \frac{1}{nj} \sum_{j=1}^{nj} \left( \frac{h}{\|\mathbf{x}_{\text{asp},i} - \mathbf{x}_{\text{asp},j}\|} \right)^{2}$$
(7)

where i and j denote two neighbouring nodes, nj is the number of nodes adjacent to i and  $\mathbf{x}_{\mathrm{asp},i} = (x,y,Z_{\mathrm{asp},i})$  indicates the coordinates of the crack asperity peak (in which x and y denote the cartesian coordinates of node i and  $Z_{\mathrm{asp},i}$  the asperity height).

To calculate the crack roughness (Equation 6), a macro-element technique is employed analogous to the method employed to distribute boundary fluxes in Ricketts et al. [39, 61]. In the present work, the macro-elements are defined such that element

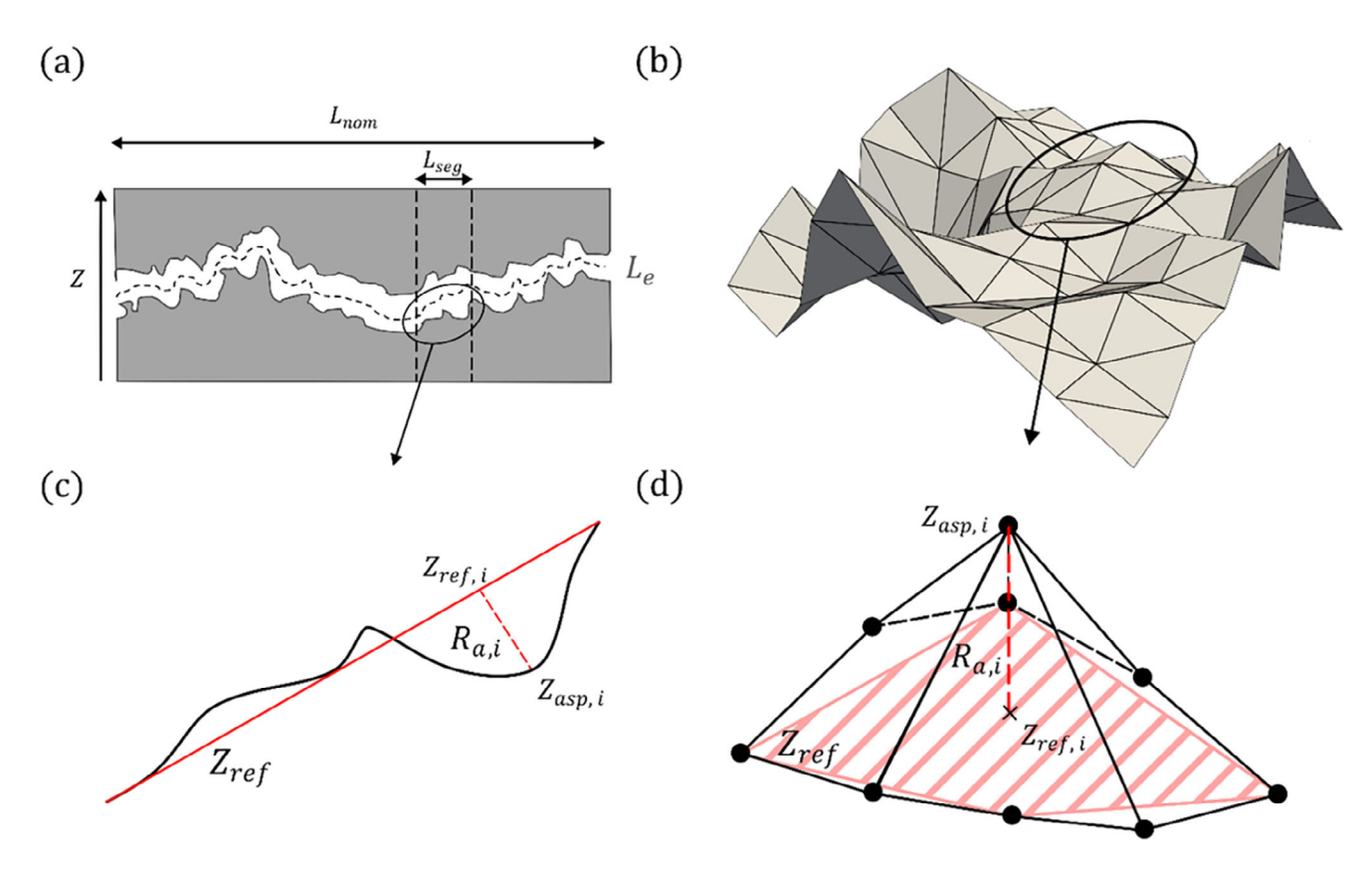


**FIGURE 2** | Illustration of crack profile showing (a) nominal and effective lengths, and a reference line for a segment of the crack profile, (b) roughness calculation in 1D, (c) 2D crack mesh showing asperities and (d) calculation of roughness in 2D.

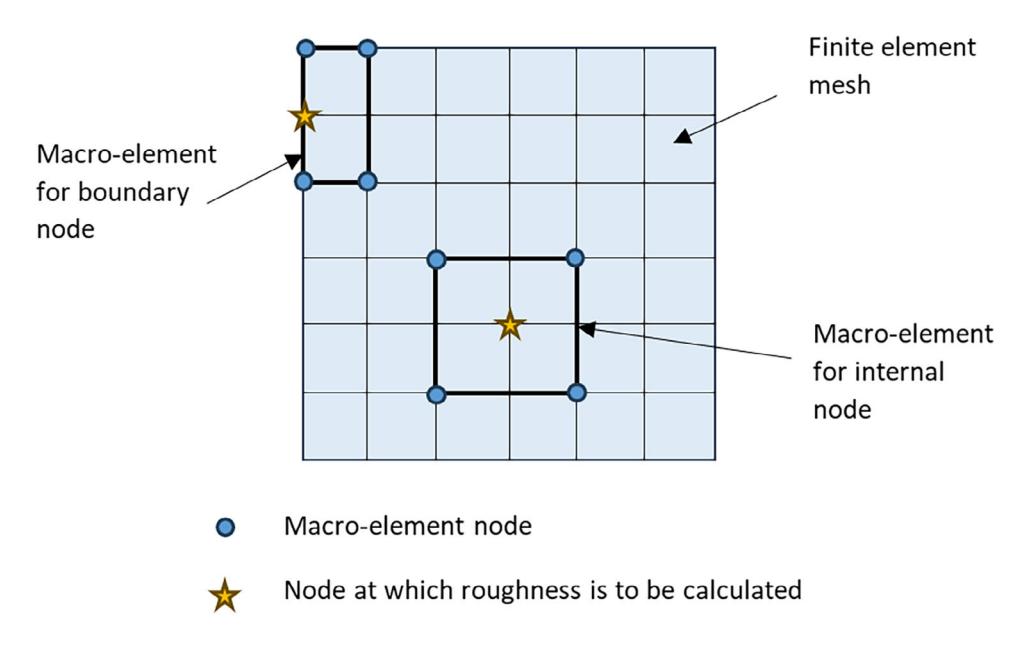


FIGURE 3 | Illustration of the macro-elements used for roughness calculation.

boundaries align with the underlying finite element mesh. A depiction of the finite element mesh, and examples of macro-elements used to calculate the roughness for internal and boundary nodes, can be seen in Figure 3.

For each macro-element, the crack roughness  $(R_a)$  for node i can be calculated as follows:

$$R_{a,i} = ||N_i Z_{\text{asp},i} - Z_{\text{ref},i}|| = ||Z_{\text{asp},i} - \mathbf{N}_m^T \mathbf{Z}_{\text{asp},m}||$$
(8)

where  $N_i$  is the shape function associated with node i (equal to 1 as  $R_{a,i}$  is evaluated at the nodal position),  $Z_{{\rm ref},i}$  is the reference asperity height at the position of node i,  $\mathbf{N}_m$  is the vector of shape functions defined on the macro-element and  $\mathbf{Z}_{{\rm asp},m}$  is the vector of macro-element nodal asperity heights.

**2.1.2.2** | **Effect on Crack Permeability.** Once the values of crack roughness and tortuosity are known, the crack permeability can be calculated according to [12, 13]:

$$K = \left(\frac{\tau}{1 + c_3 R_r^{1.5}}\right) \left(\frac{w^2}{\mu} + \frac{w\beta_w}{2}\right)$$
 (9)

where  $R_r = R_a/2w$  is the relative surface roughness and  $c_3$  is a constant typically taken equal to 8.8 [13, 15].

A key feature of the present approach is that we allow both roughness and tortuosity to vary across the domain, rather than employ a single global mean value. This, along with the use of a spatially varying crack width, enables the approach to capture the heterogeneity in the flow processes.

**2.1.2.3** | **Scale Dependence.** Experimental evidence has shown that cracks exhibit a fractal behaviour [13], in which the effective length,  $L_e$ , (and hence tortuosity), as well as roughness, depends upon the scale at which they are measured via the following relations:

$$L_e = F_{L_o} \lambda^{1-D} \tag{10}$$

$$R_a = F_{R_-} \lambda^{2-D} \tag{11}$$

where  $\lambda$  is the scale of measurement, D is the fractal dimension and  $F_{L_o}$  and  $F_{R_a}$  are constants.

In addition, noting that  $\tau = (L_{\text{nom}}/L_e)^2$  [13], the fractal relation for the tortuosity can be derived from Equation (10) as:

$$\tau = \left(\frac{L_{\text{nom}}}{F_{L_e}}\right)^2 \lambda^{-2(1-D)} \tag{12}$$

where  $L_{\mathrm{nom}}$  is the nominal (non-tortuous) crack length.

#### 2.2 | Random Field Generator

# 2.2.1 | Gaussian Random Field Representation of Concrete Crack Asperities

In the following, the theory of random field generation based on the solution of a stochastic PDE is presented [29, 62].

Let  $\mathbf{X} \in \mathbb{R}^d$  be a Gaussian random field where its contents are parameterised collections of Gaussian random variables  $\{\mathbf{X}(\mathbf{x})\}_{\mathbf{x} \in \mathbb{R}^d}$ . Here, the covariance of the field is assumed to be a function of spatial distance alone, so a standard ACF form is suitable for representing the correlation structure. The Matérn ACF is chosen, such that:

$$ACF_{X}(\mathbf{x}) = \frac{2^{1-\nu}}{\Gamma(\nu)} \left(\frac{\|\mathbf{x}\|}{l}\right)^{\nu} K_{\nu} \left(\frac{\|\mathbf{x}\|}{l}\right)$$
(13)

for  $\mathbf{x} \in \mathbb{R}^d$ , where  $\nu > 0$  is the smoothness parameter,  $\Gamma$  is the gamma function and  $K_{\nu}$  is the Bessel function of the second kind of order  $\nu$  [63]. The length-scale parameter l > 0 controls the correlation length of the resulting field, whereby  $\delta = l\sqrt{8\nu}$  is a range parameter defined as the distance at which correlations are near 0.1 for all  $\nu$  [62].

Following the approach of Roininen et al. [29], Equation (13) is approximated by posing the function as the stochastic PDE:

$$\left(1 - l^2 \Delta\right)^{\frac{(\nu + d/2)}{2}} \mathbf{X} = \sqrt{\alpha l^d} \mathbf{W}$$
 (14)

where d = 1, 2, 3, **W** is white noise on  $\mathbb{R}^d$  and  $\alpha$  is a constant such that:

$$\alpha := \sigma^2 \frac{2^d \pi^{d/2} \Gamma(\nu + d/2)}{\Gamma(\nu)}$$
 (15)

where  $\sigma$  is the standard deviation. The smoothness parameter  $\nu$  is fixed as  $\nu=2-d/2$  rendering the Equation (14) elliptic, such that:

$$(\mathbf{I} - l^2 \Delta) \mathbf{X} = \sqrt{\alpha l^d} \mathbf{W}$$
 (16)

where I is the standard identity matrix.

For a fuller description of the stochastic PDE theory and solution process, the interested reader is referred to Ricketts et al. [39].

Remark. A number of different ACFs could be used to generate the random field, including (but not limited to) the triangular and exponential type [64]. In the present work, the Matérn ACF was preferred due to its computational efficiency when combined with the approach of Roininen et al. [29]. The efficacy of the Matérn ACF at representing (quantifiably) realistic concrete cracks is both verified, using alternative software, and validated, using experimental data, in Section 4.

## 2.2.2 | Smoothed Gaussian Noise Representation of Spatially Varying Crack Width

During the fracture process, some material will be lost from each of the crack faces. As a result of this, the crack width will exhibit a spatial variation even for specimens with a nominally constant crack width. To represent the deviation of the crack width from the nominal value a zero mean Gaussian noise is generated. Following this, to match experimental observations of the crack width variation, a Gaussian smoothing is applied, before the field is scaled to the match the observed standard deviation. The scaling is based on measured values of crack width from the samples, as detailed in Appendix A.

### 2.3 | Bayesian Model Calibration

Experimental evidence shows that the correlation length and standard deviation of the crack asperities show significant variation between samples. To account for this uncertainty, as well as the uncertainty associated with experimental measurements of crack permeability (see [13]), we employ a Bayesian statistical inference to determine the probability density function (PDF) of the random field model parameters ( $\theta = [l, \sigma]$ ) [30]:

$$\pi_{\text{post}}(\boldsymbol{\theta}|\mathbf{D}) = \frac{\pi_{\text{like}}(\mathbf{D}|\boldsymbol{\theta})\pi_{\text{prior}}(\boldsymbol{\theta})}{\pi_{\text{evid}}(\mathbf{D})}$$
(17)

where  $\pi_{post}(\boldsymbol{\theta}|\mathbf{D})$  is the posterior PDF that defines the Bayesian update of the prior information  $(\pi_{prior}(\boldsymbol{\theta}))$  with the observed data

(**D**) and  $\pi_{\rm evid}(\mathbf{D}) = \int \pi_{\rm like}(\mathbf{D}|\boldsymbol{\theta})\pi_{\rm prior}(\boldsymbol{\theta})d\boldsymbol{\theta}$  is the evidence that plays the role of a normalisation factor.

In the present work the prior information relates to measurements of the correlation length and standard deviation from cracked specimens (detailed in Appendix A). The prior information is assumed to be log-normally distributed to ensure that the parameters are strictly positive.

The likelihood function found in Equation (17) is the probability of the observed data given the model output (**d**). Due to the stochastic nature of the random field model, the model output is non-deterministic for the same set of model parameters. The model output associated with a stochastic model can be represented as  $\mathbf{d}(\theta,\omega)$ , in which  $\omega$  denotes a particular model outcome from the set of all possible outcomes (see [30]). The likelihood is determined by assigning a distribution to the error between the observed data and model outcomes ( $\varepsilon$ ). Assuming the noise is additive, the error is given as  $\varepsilon = \eta + \xi = \mathbf{D} - \mathbf{d}(\theta,\omega)$ , in which  $\eta \sim \mathcal{N}(0, \Gamma_{\text{data}}^{-1})$  and  $\xi \sim \mathcal{N}(0, \Gamma_{\text{model}}^{-1})$  are the uncertainty in the observed data and model outputs, respectively.  $\Gamma_{\text{data}}$  and  $\Gamma_{\text{model}}$  represent the covariance matrices that are assumed diagonal.

Following the approach of [30], the likelihood function is given as:

$$\pi_{\text{like}}\left(\mathbf{D}|\boldsymbol{\theta}\right) = \left(\left(2\pi\right)^{2}|\boldsymbol{\Sigma}|\right)^{-0.5} \exp\left(-\frac{1}{2}(\boldsymbol{\mu}_{D} - \boldsymbol{\mu}_{d})^{T}\boldsymbol{\Sigma}^{-1}(\boldsymbol{\mu}_{D} - \boldsymbol{\mu}_{d})\right) \tag{18}$$

where  $\Sigma = \Gamma_{\text{data}} + \Gamma_{\text{model}}$  is the total covariance matrix and  $\mu_D$  and  $\mu_d$  are the vectors of means of the observed data and model outputs respectively given as:

$$\mu_D = \frac{1}{N_D} \sum_{i=1}^{N_D} D_i \tag{19}$$

$$\boldsymbol{\mu}_{d} = \frac{1}{N_{d}} \sum_{i=1}^{N_{d}} \mathbf{d}(\boldsymbol{\theta}, \omega_{i})$$
 (20)

where  $N_D$  and  $N_d$  are the number of observations and model evaluations (for a given  $\theta$ ), respectively.

#### 3 | Numerical Implementation

### 3.1 | Fluid Flow

#### 3.1.1 | Variational Formulation

Combining the mass balance and Darcy equations given in Equation (1), we obtain a Poisson problem for the pressure which is given in variational form as:

Find  $\mathbf{P} \in H^1(\Omega)$  such that:

$$\int_{\Omega} \mathbf{v} \cdot (\nabla \cdot (-\rho w \mathbf{K} \nabla \mathbf{P}))$$

$$= \int_{\Omega} \mathbf{v} \cdot \left( \nabla \cdot \rho w \rho \mathbf{g} - \frac{\partial \rho w}{\partial t} \right), \forall \mathbf{v} \in H^{1}(\Omega) \tag{21}$$

where  $\bf P$  is the solution vector and  $\bf v$  are the test functions.

### 3.1.2 | Cut Finite Element Without Cutting the Mesh

In the present work, a PCutFEM model is employed in which the mesh does not conform with the physical domain. The specific method employed is the 'CutFEM without cutting the mesh cells' proposed by Lozinski [50] and is based on the UFEM of Hansbo and Hansbo [65]. In this approach, a simple background mesh is defined  $(T_h^0)$ , into which the physical domain is embedded. The computational mesh  $(T_h)$  is obtained through the removal of all elements with zero intersection with the physical domain:

$$T_h = \left\{ T \in T_h^0 \mid T \cap \Omega \neq \emptyset \right\} \tag{22}$$

where *T* indicates an element in the mesh, and the computational domain is defined as:

$$\Omega_h = \left(\bigcup_{T \in T_h} T\right)^{\circ} \tag{23}$$

A depiction of the background mesh, physical domain and corresponding computational mesh can be seen in Figure 4.

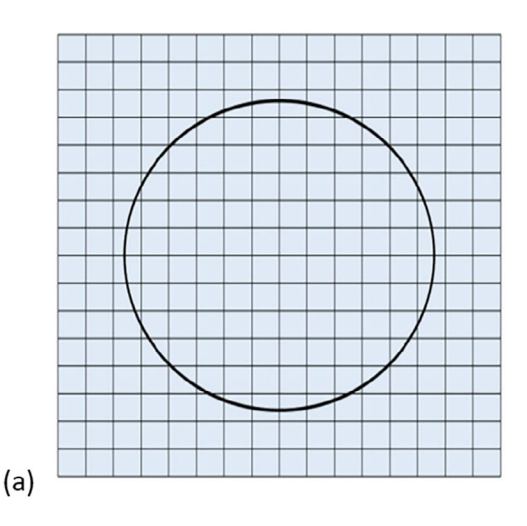
It is clear from the definition of the computational mesh that it is simply the physical domain plus some small extension (o) such that  $\Omega_h = \Omega \cup o$ . The main idea of the approach of Lozinski [50] is the assumption that the problem defined in Equation (21) can extended from the physical mesh to the computational mesh, with the boundary conditions still imposed on the physical boundary. It is noted that a similar assumption is made in Pande et al. [53] and Freeman and Jefferson [12] for a cut-cell and multi-point constraint UFEM [66], respectively. In the shifted boundary method [51], the problem is extended, and the boundary conditions imposed on a surrogate boundary. The advantage of such approaches is the avoidance of integration over cut elements, and the associated conditioning issues associated with 'bad' cuts.

Discretising Equation (21), integrating by parts over the computational mesh and employing a nonsymmetric Nitsche's method for weakly enforcing boundary conditions lead to:

Find  $\mathbf{P} \in H^1(\Omega)$  such that:

$$\int_{\Omega_{h}} \nabla \mathbf{v} \cdot \rho w \mathbf{K} \nabla \mathbf{P} - \int_{\Gamma_{h}} \mathbf{v} \cdot \rho w \mathbf{K} \frac{\partial \mathbf{P}}{\partial \mathbf{n}} + \int_{\Gamma_{f}} \frac{\partial \mathbf{v}}{\partial \mathbf{n}} \cdot \rho w \mathbf{K} \mathbf{P} 
+ \frac{\vartheta}{h} \int_{\Gamma_{f}} \mathbf{v} \cdot \mathbf{P} + \varepsilon h \sum_{E \in E_{g}} \int_{E} \left[ \left[ \frac{\partial \mathbf{v}}{\partial \mathbf{n}} \right] \right] \cdot \left[ \left[ \frac{\partial \mathbf{P}}{\partial \mathbf{n}} \right] \right] 
= \int_{\Omega_{h}} \nabla \mathbf{v} \cdot \rho w \rho \mathbf{g} - \int_{\Omega_{h}} \mathbf{v} \cdot \frac{\partial \rho w}{\partial t} + \int_{\Gamma_{f}} \frac{\partial \mathbf{v}}{\partial \mathbf{n}} \cdot \rho w \mathbf{K} \mathbf{P}_{d} 
+ \frac{\vartheta}{h} \int_{\Gamma_{f}} \mathbf{v} \cdot \mathbf{P}_{d}, \quad \forall \mathbf{v} \in H^{1}(\Omega)$$
(24)

where  $[|\mathbf{x}|] = \mathbf{x}|_{T^+} - \mathbf{x}|_{T^-}$  is the jump operator,  $\mathbf{n}$  is the outward facing normal,  $\vartheta \ge 0$  is a Nitsche penalty parameter,  $\varepsilon \ge 0$  is a ghost penalty parameter and h is a measure of the element size. The final term in the left-hand side of Equation (24) is a ghost penalty included to both stabilise the bilinear form and extend the solution from the computational mesh to the background mesh [12, 50], which is important for the level-set method introduced



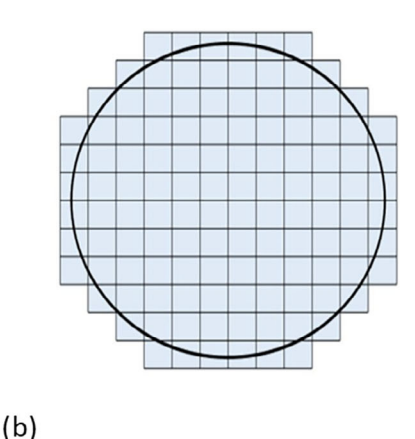


FIGURE 4 | Simple background mesh into which the domain is embedded (a), and corresponding computational mesh (b) (reproduced from Freeman [66] with permission).

in the Section 3.1.3. The ghost penalty is applied to the internal edges of the computational mesh, defined as:

$$E_{\sigma} = \{ E \in \partial T_h \mid E \cap \partial \Omega_h = \emptyset \}$$
 (25)

where E denotes an element edge,  $\partial T_h$  is the global set of element edges,  $\Omega_b$  is the background mesh domain (or crack plane) and  $\partial \Omega_b$  its boundary.

It is noted that the consistency term (the second term in the lefthand side of Equation 24) is applied over the outer boundary of the computational mesh ( $\Gamma_h$ ), whilst the terms associated with Nitsche's method are applied over the physical boundary ( $\Gamma_f$ ).

The fluid flow domain, as well as the physical boundary, and outer boundary of the computational mesh, employed in Equation (24), are determined from the level set. Mathematically, the computational domain, outer boundary and physical boundary are all functions of the level set, that is,  $\Omega_h(\Omega(\varphi))$ ,  $\Gamma_h(\Omega_h(\varphi))$  and  $\Gamma_f(\varphi)$ .

The fluid flow and level set are solved in a staggered solution procedure. The full solution algorithm can be seen in Section 3.5.

## 3.1.3 | Interface Tracking With Level-Set Method

The movement of the fluid interface is tracked by the level-set method that is given as:

$$\frac{\partial \varphi}{\partial t} + \mathbf{u} \cdot \nabla \varphi = 0 \tag{26}$$

where  $\varphi$  is the level-set that is a signed distance function with the following properties:

$$\varphi > 0 \ \forall \mathbf{x} \in \Omega_f, \ \varphi < 0 \ \forall \mathbf{x} \notin \Omega_f, \ \varphi = 0 \ \forall \mathbf{x} \in \Gamma_f$$
 (27)

where  $\Omega_f$  indicates the fluid domain.

In the present work, we employ the assumed gradient level-set (i.e., we assume that  $|\nabla \varphi| = 1$ , in which |x| indicates the absolute value of x) following the approach of [67], such that Equation (26)

can be rearranged to give:

$$\frac{\partial \varphi}{\partial t} + u_n |\nabla \varphi| = 0 \to \frac{\partial \varphi}{\partial t} + u_n = 0 \tag{28}$$

where  $u_n = \mathbf{u} \cdot \nabla \varphi / |\nabla \varphi|$  is the velocity normal to the interface.

The weak form reads:

Find  $\varphi \in H^1(\Omega)$  such that:

$$\int_{\Omega_{h}} \mathbf{v} \cdot \frac{\partial \boldsymbol{\varphi}}{\partial t} = -\int_{\Omega_{h}} \mathbf{v} \cdot \mathbf{u} \cdot \frac{\nabla \boldsymbol{\varphi}}{|\nabla \boldsymbol{\varphi}|}, \forall \mathbf{v} \in H^{1}(\Omega)$$
 (29)

The time discretisation employs a backward difference method, whilst a modified fast-marching method is employed for the level-set reinitialisation [68], which is important for maintaining the level-set as a signed distance function. Finally, the time step size was limited according to a Courant–Friedrichs–Lewy (CFL) condition given as:  $u\Delta t/h \leq C$ .

#### 3.2 | Random Field Generator

Here, the solution to Equation (16) is approximated with the FEM. This is a non-unique solution and defined over  $\mathbb{R}^d$ , and as such, boundary conditions are supplied such that the problem is well posed. The reduction of a solution in  $\mathbb{R}^d$  to a finite domain introduces spurious values in the near-boundary region, resulting in a correlation structure that differs from the rest of the domain [69]. This behaviour can be controlled though the choice of boundary condition that is applied. Although the well-known Dirichlet and Neumann conditions can be specified, here the approach of Ricketts et al. [69] is taken, supplying a weighted Dirichlet–Neumann boundary condition

$$\alpha \mathbf{X} + (1 - \alpha) l \frac{\partial \mathbf{X}}{\partial \mathbf{n}} = 0 \text{ on } \partial \Omega_b$$
 (30)

where  $\alpha \in [0, 1]$  is the weighting parameter that controls the ratio of the Dirichlet and Neumann components. This is nothing more

than a cosmetic change to the Robin condition:

$$\left(\mathbf{X} + \lambda \frac{\partial \mathbf{X}}{\partial \mathbf{n}}\right) | \partial_{\Omega_b} = 0 \tag{31}$$

where the Robin coefficient  $\lambda$  can be formulated from Equation (30) as

$$\lambda = \lambda (\alpha, l) = \frac{1 - \alpha}{\alpha} l. \tag{32}$$

Discretising Equation (16) and integrating by parts over the background mesh leads to the following weak form:

Find  $\mathbf{X} \in H^1(\Omega)$  such that:

$$\int_{\Omega_{b}} \mathbf{v} \cdot \mathbf{X} + l^{2} \int_{\Omega_{b}} \nabla \mathbf{v} \cdot \nabla \mathbf{X} + \frac{l^{2}}{\lambda} \int_{\partial \Omega_{b}} \mathbf{v} \cdot \mathbf{X}$$

$$= \sqrt{\alpha l^{2}} \int_{\Omega_{c}} \mathbf{v} \cdot \mathbf{W}, \forall \mathbf{v} \in H^{1}(\Omega) \tag{33}$$

As the generated field is merely a solution of the SPDE in  $\mathbb{R}^2$ , this allows it to represent any model parameter which should be spatially varying. Here, it is assigned to represent the geometry of the crack face, as this will have direct impact on the effective permeability of the crack, resulting in non-uniform fluid motion.

### 3.3 | Bayesian Model Calibration

To establish the posterior distribution (Equation 17), we employ a sequence of m Markov Chain Monte Carlo (MCMC) simulations. The simulations are determined using the Random Walk Metropolis–Hastings (MH) algorithm. The MH algorithm forms a Markov Chain (MC) by proposing a jump in variables from the current values through sampling candidates from a proposal distribution. The proposed jump is then accepted or rejected according to an acceptance probability. The starting point for the chain is determined by sampling variables values from an appropriate uniform distribution. For further details of the approach, the interested reader is referred to [70].

To determine the convergence of the algorithm, we follow the approach of Brooks and Gelman [71]. The method involves simulating m MCs for 2n iterations and discarding the first n to account for the burn-in period. The estimated target (posterior) mean  $(\widehat{\mu})$  and variance  $(\widehat{\sigma^2})$  are then calculated as:

$$\widehat{\mu} = \frac{1}{mn} \sum_{i=1}^{m} \sum_{j=1}^{n} \theta_{ij}$$
 (34a)

$$\widehat{\sigma^2} = \frac{n-1}{n} \mathbf{W}_v + \frac{\mathbf{B}}{n}$$
 (34b)

in which the between- and within-chain variances ( $\mathbf{B}/n$  and  $\mathbf{W}_v$ , respectively) are given as:

$$\mathbf{B}/n = \frac{1}{m-1} \sum_{i=1}^{m} \left( \overline{\theta_j} - \widehat{\mu} \right)^2$$
 (35a)

$$\mathbf{W}_{v} = \frac{1}{m(n-1)} \sum_{i=1}^{m} \sum_{j=1}^{n} \left( \boldsymbol{\theta}_{ij} - \overline{\boldsymbol{\theta}_{j}} \right)^{2}$$
 (35b)

in which the overbar denotes the mean value.

Finally, using the above, the potential scale reduction factor  $(\hat{\mathbf{R}})$  can be calculated as:

$$\widehat{\mathbf{R}} = \frac{m+1}{m} \frac{\widehat{\sigma}^2}{\mathbf{W}_n} - \frac{n-1}{mn} \tag{36}$$

A value of  $\hat{\mathbf{R}}$  near to one gives an indication that each of the simulated MCs had converged to the target (posterior) distribution [71].

#### 3.4 | Random Number Generators

In the present work, the white noise vector utilised in the random field model, as well as the zero mean Gaussian noise used in the representation of the spatially varying crack width, was generated using the DLARNV subroutine from the FORTRAN linear algebra package, LAPACK. The seeds sampled for the random field model, as well as the samples used in the MH algorithm (e.g., from the proposal distribution), were generated using the numpy.random module from the NumPy Python package. The performance of numerical algorithms as well as the convergence of statistical properties can be significantly affected by the quality random number generators [72]. Although a number of methodologies for the assessment of the quality of random number generators have been proposed (see, e.g. [73, 74]), such an assessment is beyond the scope of this study.

#### 3.5 | Algorithm

The solution scheme can be seen in Box 1 that shows how the model components fit together.

#### 4 | Generation of Virtual Rough Fractures

Before applying the model to an example problem, the performance of the random field model for generating virtual rough fractures is demonstrated. To this end, a series of cracks generated using an alternative software package, as well as experimental measurements on crack profiles and permeability are considered.

## 4.1 | Virtual Fractures From Synfrac

In the present example, we consider the series of cracks presented in Yin et al. [75]. The cracks considered were 100 mm in width and 100 mm in length and were generated using the well-established, and validated, software package Synfrac [20]. In their study, Yin et al. [75] varied the fractal dimension  $(D_f)$  and standard deviation to generate cracks with different roughness characteristics. To allow a direct comparison of the results of the present model with those presented in Yin et al. [75], we consider the  $Z_2$  factor proposed by Myers [76] and used by Yin et al. [75] to quantify the crack roughness of the generated fractures.

SOX I   Solution algorithm	
Calculate $\pi_{\text{post}}(\boldsymbol{\theta} \mathbf{D})$	Calculate posterior distribution using Metropolis–Hasting's algorithm and random field model (Section 3.3)
For $ireal = 1$ to $nreal$	Start loop over number of realisations
Let $Y_{14} \sim U$ such that $Y_4$ is odd	Sample seed numbers for random field model and smoothed Gaussian noise from a uniform distribution
Let $\theta_{12} \sim \pi_{\text{post}}(\boldsymbol{\theta} \mathbf{D})$	Sample random field model parameters from posterior distribution
Solve for <b>X</b>	Solve the random field model for crack asperities (Equation 33)
Calculate ${f R}_a$ and ${f  au}$	Calculate roughness and tortuosity from crack geometry (Equations 7 and 8)
Scale $\mathbf{R}_a$ and $\boldsymbol{\tau}$ using fractal relationship	Calculate roughness and tortuosity at considered length scale (Equations 11 and 12)
$t=t_0$ , $oldsymbol{arphi}=oldsymbol{arphi}_0$	Initialise cumulative variables (time and level-set)
For $i$ time = 1 to $n$ time	Start time step loop
$t_{i \text{time}} = t_{i \text{time}-1} + \Delta t$	Set time variable
Solve for <b>P</b>	Solve flow problem (Equation 24)
Calculate $m{u}$	Calculate velocity from pressure field (Equation 1b)
Solve for $\varphi$	Solve level-set movement (Equation 29)
End for itime	End time step loop
End for ireal	End loop over realisations
Calculate CI and CL of results	Calculate mean rise heights, confidence intervals and confidence level of results

**TABLE 1** Correlation lengths employed in the random field model.

Fractal dimension $D_f$ (-)	Correlation length l (mm)
1.2	29.1
1.6	25.8
2.0	11.7
2.4	3.6

The  $Z_2$  factor is given by:

$$Z_{2} = \sqrt{\frac{1}{N_{x}\Delta x N_{y}\Delta y} \sum_{j=1}^{N_{x}} \sum_{i=1}^{N_{y}-1} (z_{j,i+1} - z_{j,i})^{2}}$$
(37)

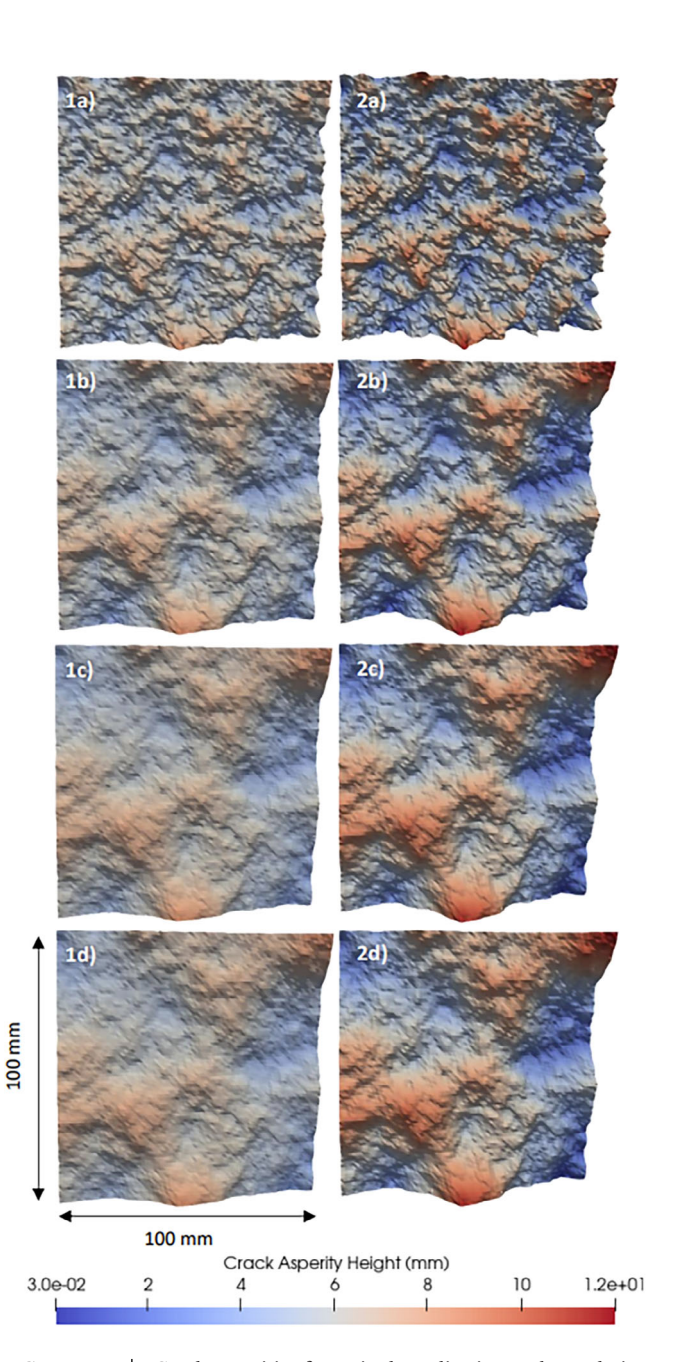


**FIGURE 5** | Crack asperities for a single realisation and correlation lengths of 3.6 mm (a), 11.7 mm (b), 25.8 mm (c) and 29.1 mm (d) and standard deviation of 1 mm (1) and 2 mm (2).

where  $N_x$  and  $N_y$  are the number of divisions in x and y, respectively,  $\Delta x$  and  $\Delta y$  are the distance between adjacent points in x and y, respectively and  $z_{j,i}$  is the asperity height of the point (j,i).

For the random field model, it was assumed that the crack faces were complementary such that a single random field generation of crack asperities could be employed to represent both crack faces. For each set of random field parameters ( $\theta$ ), five different realisations were generated. The mean asperity height was set to 15 mm, it is noted that the roughness and tortuosity that affect the fluid flow are a function of the relative asperity heights (see Equations 7 and 8) and, as such, are unaffected by the absolute value. The correlation lengths were calibrated to match the results of Yin et al. [75].

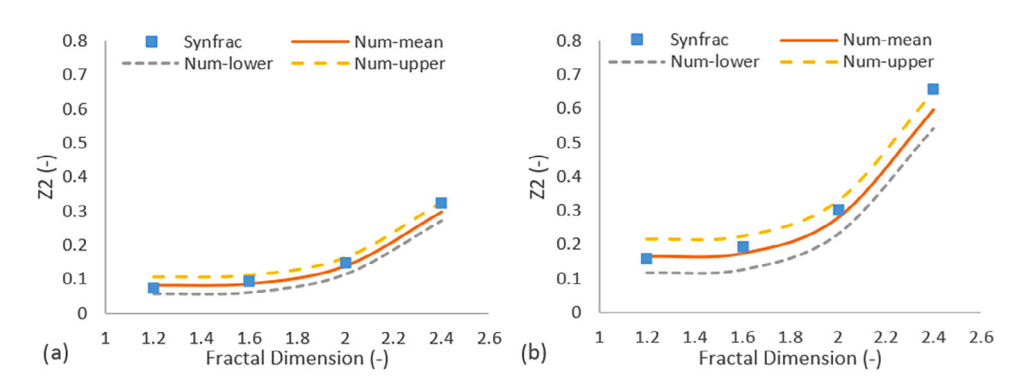


**FIGURE 6** Comparison of numerical results and those presented in [75] for standard deviations of 1 mm (a) and 2 mm (b) in which the numerical results show the mean and 95% confidence intervals.

**TABLE 2** | Comparison of crack profile characteristics.

Mix	Parameter	Exp. mean	Exp. STD	Num. mean	Num. STD
NC	τ (-)	0.8995	0.0249	0.9067	0.0220
	$R_s(-)$	1.1534	0.0596	1.0999	0.0260
PPRC4	τ (-)	0.8707	0.0348	0.8764	0.0239
	$R_s(-)$	1.1979	0.0484	1.1374	0.0305
PPRC6	τ (-)	0.8536	0.0213	0.8467	0.0264
	$R_s(-)$	1.2172	0.0428	1.1775	0.0363

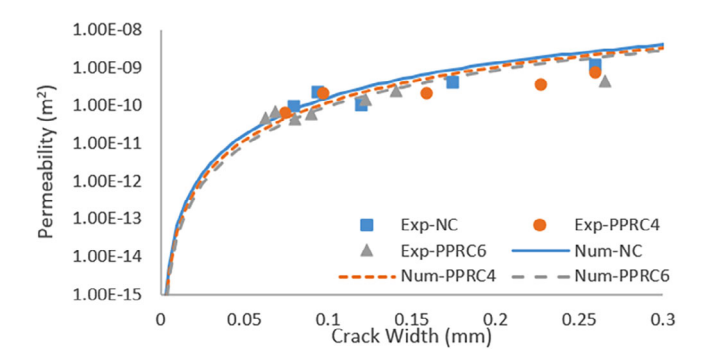


**FIGURE 7** Comparison of predicted permeability with experimental data presented in [77].

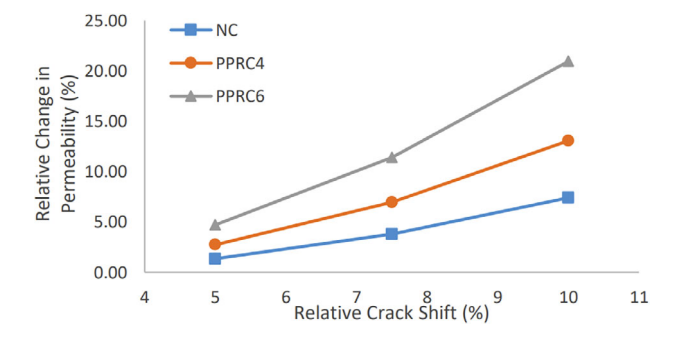


FIGURE 8 | Effect of crack shift on predicted permeability.

The correlation lengths used in the present model for each of the fractal dimensions can be seen in Table 1. It is noted that both the present model and Synfrac use the standard deviation, and as such, the values given in Yin et al. [75] could be used directly.

The generated cracks for a single realisation can be seen in Figure 5. The effect of correlation length and variability can clearly be seen in the generated fields. Those associated with higher correlation lengths and lower SDs exhibit a smoothly varying crack face; whilst those associated with lower correlation lengths and higher SDs show significant variations in crack asperity height and a roughly varying crack face.

A comparison of the roughness characteristics of the generated cracks, and those presented in Yin et al. [75], can be seen in Figure 6. The numerical results shown correspond to the mean and 95% confidence intervals (CIs), calculated using the using the *t*-distribution due to the small sample size. It can be seen from the figure that there is good agreement between the results of the present model, and those presented in Yin et al. [75].

# **4.2** | Experimental Measurements of Concrete Fractures

In this example, which validates the random field model, and roughness and tortuosity calculations, we consider the experimental data presented in Li and Liu [77] that consisted of both measurements of crack roughness and tortuosity, and crack permeability of normal and polypropylene fibre reinforced concrete.

### 4.2.1 | Crack Profiles

A number of samples of a normal concrete (NC) mix and two polypropylene fibre reinforced concrete mixes (PPRC4 and

**TABLE 3** | Mix proportions for concrete specimens.

Designation	Cement <sup>a</sup> (kg/m <sup>3</sup> )	Fine aggregate <sup>b</sup> (kg/m³)	Coarse aggregate <sup>c</sup> (kg/m <sup>3</sup> )	Water (kg/m³)	Compressive strength (CoV) (N/mm <sup>2</sup> ) (%)
C50	416.7	808.3	1008.3	166.7	44.6 (2.9)

aCEM IV/B-V 32,5R.

<sup>&</sup>lt;sup>c</sup>Max aggregate size 10 mm crushed limestone.

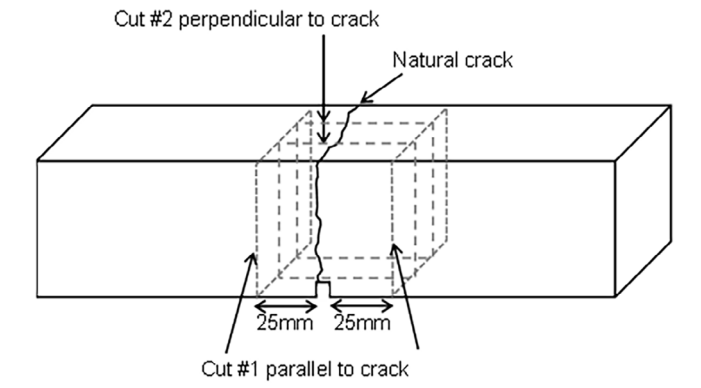


**FIGURE 9** | Specimen manufacture from concrete prisms.





**FIGURE 10** | Natural crack profiles for tap water (TW) specimens (a) and ground-granulated blast furnace slag (GGBS) in suspension specimens (b).

PPRC6) were analysed by Li and Liu [77], for which the tortuosity and surface roughness factors were calculated. The surface roughness  $(R_s)$  was defined as the ratio of actual crack area  $(A_{crk})$  to the projected crack area (i.e., the nominal area of the crack,  $A_{nom} = L_x L_y$  in which  $L_x$  and  $L_y$  indicate the length of the crack in the x and y direction, respectively).

Cracks of 75 mm in width and 75 mm in length were generated. For the random field model, it was assumed that the crack faces were complementary such that a single random field generation of crack asperities could be employed to represent both crack faces. For each set of random field parameters ( $\theta$ ), five different realisations were generated. The correlation lengths and standard deviations were calibrated for each mix to match the results of Li and Liu [77].

**TABLE 4** Statistical parameters of prior and observed data distributions.

Distribution	Parameter (units)	Mean	SD
Prior	ln(l)(ln(m))	-4.054	0.508
	$\ln(\sigma)(\ln(m))$	-6.719	0.258
Observed data	$ln(R_a)(ln(m))$	-18.110	2.840
	$ln(\tau)(-)$	-1.574	0.595

The results of the comparison are given in Table 2. It can be seen from the table that the mean surface roughness and tortuosity are accurately reproduced by the numerical model. In addition, there is good agreement between the standard deviation of the tortuosity predicted by the model to that of the experimental data, whilst the surface roughness standard deviation is underpredicted.

The correlation lengths used for each mix were 8.8, 6.2 and 4.8 mm for the NC, PPRC4 and PPRC6, respectively, whilst a standard deviation of 2 mm was used for all mixes.

#### 4.2.2 | Crack Permeability

In addition to measurements of crack profiles, Li and Liu [77] also presented measurements of crack permeability for each concrete mix. To compare the predictions of the numerical model with the experimental data, the mean tortuosity and roughness (calculated at a length scale of 1000  $\mu$ m) from the numerical results for each concrete mix were used to calculate the intrinsic permeability  $(K_{\rm int} = \tau w^2/(1+8.8R_r^{1.5}))$  of the concrete cracks for a range of crack widths.

The results of the comparison are given in Figure 7. It can be seen from the figure that the numerical predictions are in good agreement with the experimental results, though the difference between the concrete mixes is less pronounced.

## 4.2.3 | Shifted Cracks - The Advantage of the Consideration of Heterogeneity and Crack Asperities

This example was also used to demonstrate one of the key advantages of the consideration of the heterogeneity of the flow processes and crack asperities, namely, capturing the effect of crack sliding. In concrete structures, cracks are subject to shear displacements in addition to the normal crack opening displacements. For rough and non-planar cracks, this leads to local deviations from the nominal crack opening. Such local

<sup>&</sup>lt;sup>b</sup>4 mm max marine dredged sand.

10969853, 0, Downle

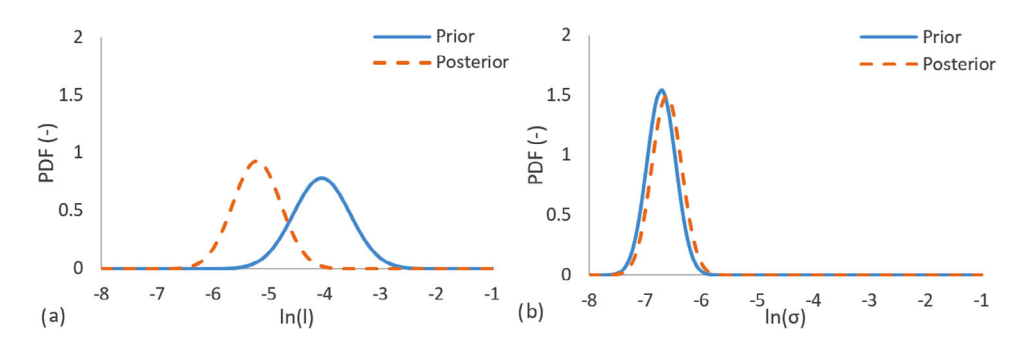


**FIGURE 11** Prior and posterior distributions for (a) ln(l) and (b)  $ln(\sigma)$ .

**TABLE 5** | Statistical parameters of posterior distributions.

Distribution	Parameter (units)	Mean	SD
Posterior	ln(l)(ln(m))	-5.217	0.428
	$ln(\sigma)(ln(m))$	-6.624	0.266

**TABLE 6** | Fluid flow model parameters.

Model parameter (units)	TW	GGBS suspension
$\rho$ (kg/m <sup>3</sup> )	1000.0 <sup>a</sup>	1358.0 <sup>a</sup>
$\mu$ (Ns/m <sup>2</sup> )	0.00142 <sup>a</sup>	0.0032 <sup>a</sup>
$\gamma (N/m)$	0.0722 <sup>a</sup>	0.0499 <sup>a</sup>
$\theta_s$ (rad)	0.4328 <sup>a</sup>	0.4904 <sup>a</sup>
$\beta_s$ (-)	0.0 <sup>b</sup>	0.0 <sup>b</sup>
$\beta_m  (\mathrm{Ns/m^2})$	0.0 <sup>b</sup>	0.0 <sup>b</sup>
$\beta_w$ (m <sup>3</sup> /Ns)	0.0125 <sup>b</sup>	0.0125 <sup>b</sup>
<i>c</i> <sub>1</sub> (-)	1.325 <sup>b</sup>	1.325 <sup>b</sup>
<i>c</i> <sub>2</sub> (-)	0.35 <sup>b</sup>	0.35 <sup>b</sup>
<i>c</i> <sub>3</sub> (-)	8.8 <sup>c</sup>	8.8 <sup>c</sup>
θ (-)	$1^d$	1 <sup>d</sup>
€ (−)	0.001 <sup>d</sup>	0.001 <sup>d</sup>

<sup>&</sup>lt;sup>a</sup>Taken from [84].

deviations in crack width can lead to channel flow that has been shown to be characterised by effective crack permeabilities that deviate from parallel plate theory [78]. To demonstrate this effect, we consider the effect of shear displacements on the effective permeability predicted by the model for the concrete mixes presented in Li and Liu [77]. The effective permeability  $(K_{\rm eff})$  is given by:

$$K_{\rm eff} = u_{\rm av} \mu / P_{\rm grad} \tag{38}$$

where  $P_{\rm grad}$  is the applied pressure gradient and  $u_{\rm av}$  is the average velocity predicted by the numerical model (Equation 24).

The results of the investigation can be seen in Figure 8. The results show that the effect of shear displacements on the effective permeability is significant (up to 20.94% difference) and that the effect is more significant for more tortuous and rough cracks (see values for each mix in Table 2).

## 5 | Flow Through Concrete Fracture

In this section, to validate the proposed model, the flow through a concrete fracture is considered. The example concerns the flow of both TW and a GGBS suspension that was first tested experimentally. In addition to comparing the results of the experiments and numerical simulations, a statistical analysis is undertaken of the model results. The statistical analysis allows the quantification of the confidence level in the numerical results.

### 5.1 | Experimental Procedure

The capillary rise of healing agents in discrete cracks has previously been reported by Gardner et al. [79, 80]. In the current study, the capillary rise of TW and water carrying GGBS powder in suspension was measured in natural discrete cracks formed in a series of concrete specimens. Concrete prisms of dimensions 75 mm  $\times$  75 mm  $\times$  255 mm were cast using the mix proportions and materials presented in Table 3. After 7 days of curing in water, the prisms were notched to a depth of 5 mm and tested until failure in three-point bending. Three pairs of test specimens were extracted from each prism by first making a cut 25 mm either side of the notch, parallel to the crack (Cut #1) and subsequent cuts perpendicular to the crack at 25 mm intervals (Cut #2), as shown schematically in Figure 9.

Pressurised air was blown over the crack surfaces to remove any loose debris. Images of the natural cracks, shown Figure 10, were then taken to establish crack length and identify surface asperities. Specimens were then soaked in water for 24 h before testing to achieve a 'saturated' state.

Three crack widths of 0.1, 0.2 and 0.3 mm were created by placing metal spacers of thickness equal to the desirable crack width along the length of the natural crack and clamping the two halves of the specimens together. Five measurements of crack width were taken along the length of the crack on the front face and rear face of the specimens to confirm the final crack width. The

<sup>&</sup>lt;sup>b</sup>Taken from or in-line with values in [54].

<sup>&</sup>lt;sup>c</sup>Taken from [13].

dTaken from [50].

10969853, 0, Down

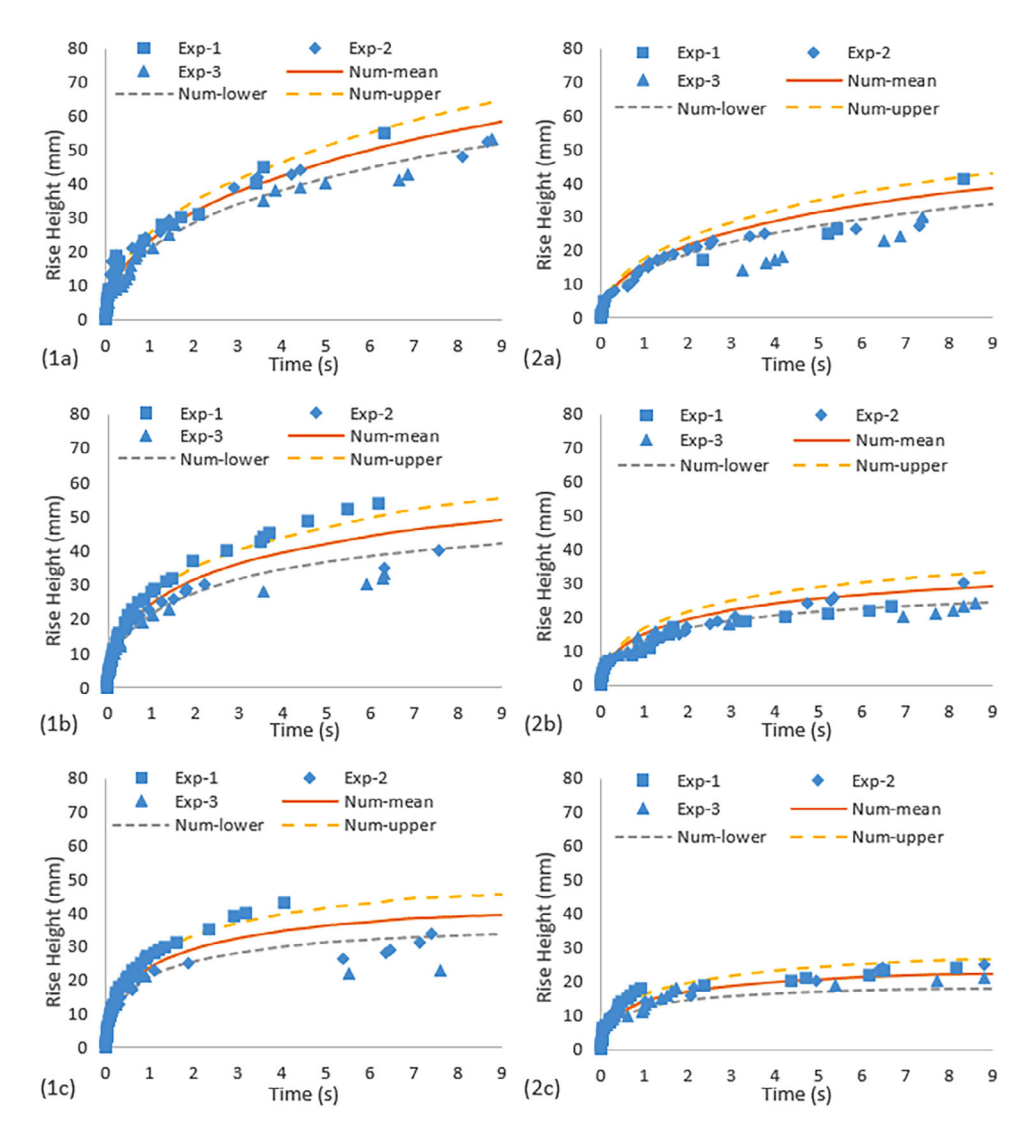


FIGURE 12 | Experimental and numerical results concerning flow of tap water (TW) (1) and ground-granulated blast furnace slag (GGBS) suspension (2) through concrete cracks of width 0.1 mm (a), 0.2 mm (b) and 0.3 mm (c) in which the numerical results show the mean and 95% confidence intervals.

clamped assembly was then fixed to a frame, such that it was suspended 10 mm above a Petri dish placed on a small hydraulic platform.

The capillary rise was captured with an AOS technologies high speed MOTIONeer camera, placed 300 mm in front of the specimens and with a recording speed of 250 frames per second. A metal scale was adhered to one side of the crack on the front face of the specimens. On commencement of recording, 50 mL of water (W) at room temperature (21°C) was poured into the Petri dish and the Petri dish raised until the bottom 0.5 mm of the specimens were submerged. This insured that contact of the base of the crack with the water occurred uniformly and at the same time across the width and breadth of the crack. Experiments ceased typically within 180 s, after no further capillary rise was observed or the capillary rise reached the full height of the specimens. The final rise height at 180 s was recorded visually, and the high-speed camera video files were then examined to track the movement of the meniscus with time.

For the capillary rise experiments with GGBS, a suspension of 60:40 water:GGBS powder (by mass) was formed and shaken for 60 s to ensure good dispersion of the powder in the water. Fifty milliliters of this suspension was added to the Petri dish, and the same procedure as noted previously was used to record the capillary rise response.

The determination of the correlation lengths of the cracked specimens, as well as the fractal parameters required for the roughness and tortuosity, is detailed in Appendix A.

# 5.2 | Bayesian Calibration of Gaussian Random Field Model

## 5.2.1 | Prior Distribution and Observed Data

To calibrate the parameters of the random field model, we employ a Bayesian approach as described in Section 2.3. The prior distribution was determined based on measurements of the

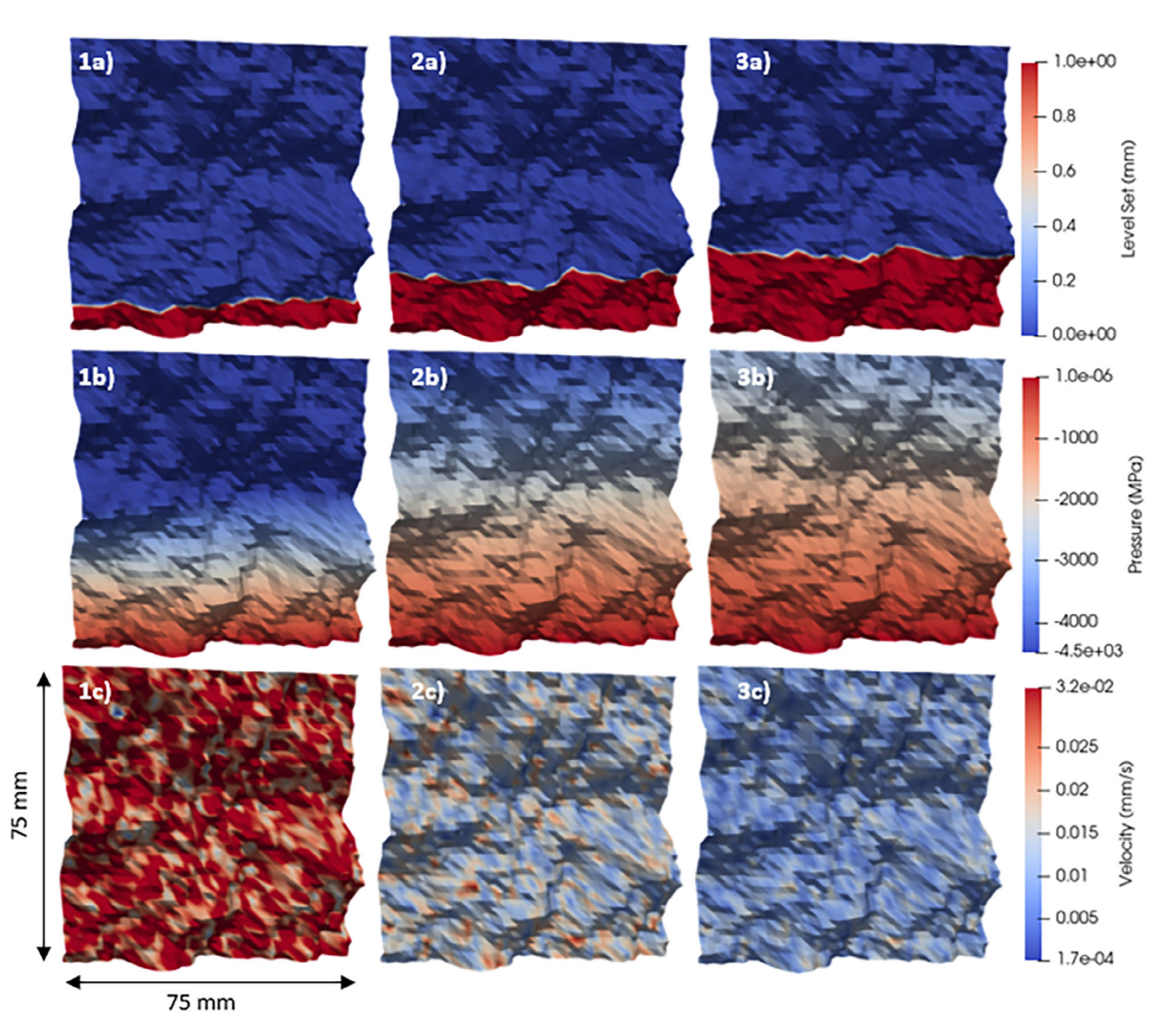


**FIGURE 13** Contours of level-set (a), pressure (b) and velocity field (c) at times t = 0.1 s (1), t = 0.5 s (2), and t = 1 s (3) for case 0.1 tap water (TW) for a single realisation.

field correlation length and standard deviation taken on cracked cementitious specimens as shown in Appendix A. It was assumed that the parameters were log-normally distributed such that the values were strictly positive.

The initial correlation length and standard deviation were sampled from the uniform distributions U[-6.9,-2.3] and U[-9.2,-4.6], respectively (that correspond to parameter values of  $l \in [1,100)$  and  $\sigma \in [0.1,10)$  in mm). The standard deviation of the proposal distribution was calibrated such that the average acceptance rate of the algorithm was close to the theoretical optimal rate [81]. The calibration resulted in a standard deviation of 1.5 times the standard deviation of the prior distribution. The number of MCs considered was 9, each of which comprised 5000 samples, a burn in of 50% (following the approach of [71]) and a 0 lag (noting that according to [82] thinning of MCs is often unnecessary).

The observed data (**D**) was related to experimental measurements of crack permeability from [13]. To relate these measurements to

observations of roughness and tortuosity, the following steps were taken: (i) the fractal dimension and constants in Equations (10) and (12) were determined based on image analysis of the cracked cementitious specimens (Appendix A) and (ii) using Equations (9), (11) and (12), the length-scale – and in-turn the roughness and tortuosity – was calibrated such that the predicted permeabilities matched the experimental values. The distribution of observed data was assumed to be log-normal such that the values were strictly positive. The statistical parameters of the prior distribution and observed data can be seen in Table 4. The length-scale used to fit the crack permeability measurements was 0.591 µm.

## 5.2.2 | Posterior Distribution and Credible Intervals

A plot of the prior and calculated posterior distributions for each of the parameters can be seen in Figure 11, whilst the statistical parameters can be seen in Table 5. The overall acceptance rate of the sampling procedure of the MH algorithm was 0.251, which is near to the theoretically optimal rate of 0.234 [81].

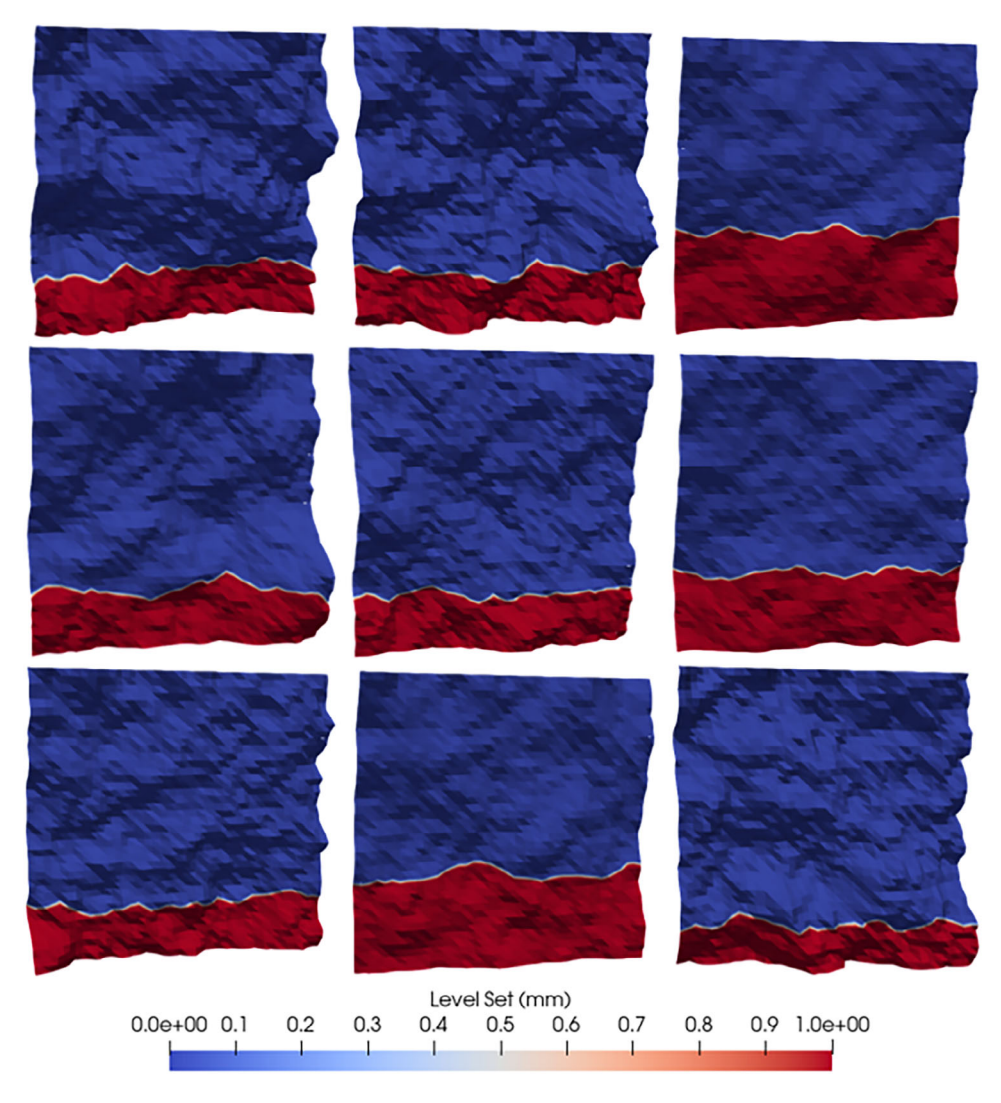


**FIGURE 14** Contours of level-set at time t = 0.5 s for Realisations 1–9, shown left to right, top to bottom, of crack asperities for case 0.1 tap water (TW).

It can be seen from Figure 11 that the posterior distribution is significantly different from that of the prior for the correlation length. The standard deviation, in contrast, shows very little difference between the posterior and prior distributions. This indicates that the initial distribution of standard deviations also provides a good fit for the observed data. In addition, the figure shows that there is greater uncertainty in the correlation length than the standard deviation of the field.

The 95% credible intervals were calculated as 2.34mm  $\leq l \leq$  12.55mm and 0.79mm  $\leq \sigma \leq$  2.24mm.

The  $\hat{R}$  scores for the correlation length and standard deviation were 1.01 and 1.00, respectively, as such, the algorithm could be considered converged [71].

## 5.3 | Numerical Simulation

The numerical simulation consisted of nine realisations of concrete cracks. For each realisation, the random field parameters

(namely the correlation length and standard deviation) were obtained by sampling the posterior distribution. The length-scale considered for the calculation of the crack tortuosity and roughness was 0.591  $\mu m$ , which was the average value obtained from fitting to the experimental data [13] and that which was employed in the Bayesian model calibration. This length scale is closely related to the scale of the concrete pores [83]. The fractal dimension was taken as 1.095, as measured from the experimental data. For the spatially varying crack width, a bandwidth of 0.9375 mm was employed in the Gaussian smoothing algorithm. The standard deviation was determined from image analysis on the cracked cementitious specimens to be 27.15% of the nominal crack width.

The tortuosity and roughness used in the calculations were determined as follows: (i) the roughness and tortuosity values were calculated according to Equations (7) and (8), (ii) for each node in the finite element mesh, Equations (11) and (12) were re-arranged to give the constants  $F_{L_e}$  and  $F_{R_a}$  and (iii) using the constants, Equations (11) and (12) were used to calculate the roughness and tortuosity values at the considered length-scale.

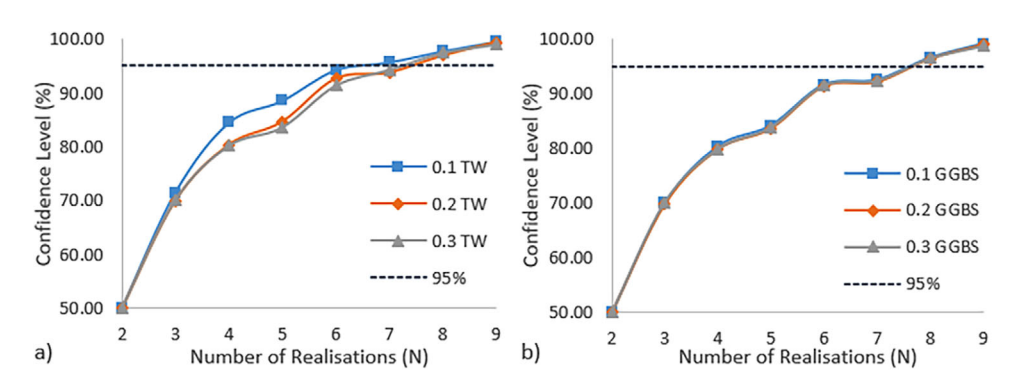


FIGURE 15 | Confidence level for mean rise height with increasing number of realisations for tap water (TW) (a) and ground-granulated blast furnace slag (GGBS) (b).

Depictions of the generated crack asperities, spatially varying crack width, and calculated roughness and tortuosity's can be seen in Appendix B.

The finite element mesh employed consisted of elements of size h = 1.875mm, chosen following a mesh convergence study, whilst the time step size was chosen to satisfy the CFL condition as detailed in Section 3. The model parameters can be seen in Table 6.

In addition to comparing the numerical results with the experimental data and noting that the numerical results depend upon the random realisation of the crack asperities and crack width variation, the confidence level in the numerical results can be established. Assuming that the mean rise heights are normally distributed and using the t-distribution due to the small sample size, the CI can be calculated (see, e.g. [38, 39]). In order to calculate realistic CIs, samples in which the rise heights deviated significantly from the mean, defined here as samples for which the median absolute deviation (MAD) was greater than 4, were discarded (see [85] for details). To avoid bias, it was ensured that the number of samples discarded from the upper and lower ends of the range was equal [85]. The mean rise height and CIs were calculated using the k = n Winsorized mean and Winsorized variance [85], where k corresponds to the number of samples removed from the upper and lower ends of the sample (see [85]).

### 5.4 | Results and Discussion

#### 5.4.1 | Experimental and Numerical Results

The results of the experiments and numerical simulations can be seen in Figure 12. The numerical results shown correspond to the k=2 Winzorised mean and 95% CIs as it was found that two samples exhibited an MAD greater than 4.

The figure shows that both the crack width and fluid properties have a significant effect on the capillary rise response. In addition, there is significant variability in the results, particularly in the case of TW. The numerical simulations are in good agreement with the experimental measurements in terms of both the mean rise height response, and the variability. As with the experimental

measurements, the TW results show greater variability that the GGBS suspension results.

An indication of the transient behaviour represented by the model can be seen in Figure 13, which shows the evolution of the level-set (representing the fluid interface), pressure and velocity field for times t=0.1–1 s for a single realisation. The figure shows that the flow front exhibits heterogeneity that evolves as the front advances through the crack. It can be seen from the figure that the velocity field shows a much greater degree of heterogeneity than the pressure field. The figure also shows that the pressure gradient and, in turn, the magnitude of the velocity is reducing with time as the body forces of the fluid begin to balance the capillary pressure at the fluid front. It is noted that the results presented include the extension of the solution from the fluid domain to the background mesh and that the fluid pressure within the fluid domain is bounded by the capillary pressure (i.e., it does not reach values of -4500 MPa as the scale in Figure 13 may suggest).

The rise height for the crack realisations at time  $t=0.5\,\mathrm{s}$  can be seen in Figure 14. It can be seen from the figure that there is a significant difference in rise heights between the realisations, with the smoother cracks (i.e., those that are less rough and tortuous) generally exhibiting greater rise heights than their rough counterparts. In addition, the figure shows that the rise heights show significant heterogeneity for each realisation, with the rougher cracks exhibiting greater heterogeneity than their smooth counterparts. The consideration of this heterogeneity is of key importance for a range of problems including self-healing concrete, in which the mechanical healing at a point within the crack is proportional to a local filling fraction [6, 11, 12].

## 5.4.2 | Statistical Analysis

To quantify the uncertainty in the results, a statistical analysis was undertaken, following the approach of Ricketts et al. [39]. The confidence level in the numerical predictions of the mean rise height using all the samples, can be seen in Figure 15. The figure shows that a confidence level of 95% is achieved within just eight simulations and that the overall trend is similar for both TW and GGBS, and the different crack widths considered. This study suggests that the number of samples required to reach a certain

confidence level can be determined by conducting successive analyses until the confidence level is achieved [39].

## 6 | Concluding Remarks

In this study, a PCutFEM with a stochastic random field generator for the simulation of flow through rough cracks has been presented. The method employs a Gaussian random field representation of crack asperities from which the crack roughness and tortuosity - both of which significantly affect the flow behaviour are calculated. In addition, to account for material loss during the fracture process, a smoothed Gaussian noise representation of the spatially varying crack width was employed. Such an approach avoids the need for empirical reduction factors and relies solely on the statistical parameters that describe the crack geometry. The statistical parameters were determined via a Bayesian statistical inference that accounted for the uncertainty in the measured values, experimental observations of crack permeability and the stochastic nature of the random field model. In addition to the distributions of the correlation length and standard deviation that describe the crack geometry, credible intervals were provided.

To demonstrate the performance of the model, new experimental data concerning the flow of TW and a GGBS suspension through concrete fractures were considered. The results show that the model was able to accurately reproduce the observed mean flow behaviour, as well as the uncertainty in the predicted rise heights. Finally, a statistical analysis was performed that quantified the confidence level in the results of the numerical simulations. The results showed that a confidence level of 95% was achieved within eight simulations.

#### **Author Contributions**

Brubeck Lee Freeman: conceptualisation, numerical investigation, methodology, writing – original draft, writing – review and editing. Evan John Ricketts: conceptualisation, numerical investigation, methodology, writing – original draft, writing – review and editing. Diane Gardner: experimental investigation, writing – original draft, writing – review and editing, funding acquisition. Anthony Jefferson: writing – review and editing, funding acquisition, supervision. Peter John Cleall: writing – review and editing, funding acquisition, supervision. Pierre Kerfriden: writing – review and editing, supervision.

### Acknowledgements

The authors thank the financial support from the EPSRC Grant EP/P02081X/1 'Resilient materials for life (RM4L)' and the finite element company LUSAS (www.lusas.com).

#### **Conflicts of Interest**

The authors declare no conflicts of interest.

### **Data Availability Statement**

The data that support the findings of this study are openly available in Cardiff University data catalogue at http://doi.org/10.17035/cardiff. 27605592.

#### References

- 1. L. Rybach, "Geothermal Power Growth 1995–2013 A Comparison With Other Renewables," *Energies* 7, no. 8 (2014): 4802–4812, https://doi.org/10.3390/en7084802.
- 2. Z. Zhong, X. Meng, Y. Hu, F. Zhang, F. Wu, and G. Wang, "Quantitative Assessments on Fluid Flow Through Fractures Embedded in Permeable Host Rocks: Experiments and Simulations," *Engineering Geology* 327 (2023): 107341, https://doi.org/10.1016/j.enggeo.2023.107341.
- 3. P. H. Stauffer, H. S. Viswanathan, R. J. Pawar, and G. D. Guthrie, "A System Model for Geologic Sequestration of Carbon Dioxide," *Environmental Science and Technology* 43, no. 3 (2009): 565–570, https://doi.org/10.1021/es800403w.
- 4. T. Meng, M. Lifeng, W. Fengbiao, F. Gan, and X. Yongbin, "Experimental Study on Permeability Evolution and Nonlinear Seepage Characteristics of Fractures Rock in Coupled Thermos-Hydraulic-Mechanical Environment: A Case Study of the Sedimentary Rock in Xishan Area," *Engineering Geology* 294, no. 5 (2021): 106339, https://doi.org/10.1016/j.enggeo.2021.106339.
- 5. A. Al-Ameeri, M. I. Rafiq, O. Tsioulou, and O. Rybdylova, "Impact of Climate Change on the Carbonation in Concrete Due to Carbon Dioxide Ingress: Experimental Investigation and Modelling," *Journal of Building Engineering* 44 (2021): 102594.
- 6. M. Rajczakowska, I. Tole, H. Hedlund, K. Habermehl-Cwirzen, and A. Cwirzen, "Autogenous Self-Healing of Low Embodied Energy Cementitious Materials: Effect of Multi-Component Binder and Crack Geometry," *Construction and Building Materials* 376 (2023): 130994, https://doi.org/10.1016/j.conbuildmat.2023.130994.
- 7. C. Zeng, Z.-S. Zheng, Y.-J. Huang, and H. Zhang, "Chloride-Induced 3D Non-Uniform Corrosion of Steel in Reinforced Concrete Considering Mesoscale Heterogeneities and Early-Age Cracks," *Construction and Building Materials* 409 (2023): 133778, https://doi.org/10.1016/j.conbuildmat.2023.133778.
- 8. N. De Belie, E. Gruyaert, A. Al-Tabbaa, et al., "A Review of Self-Healing Concrete for Damage Management of Structures," *Advanced Materials Interfaces* 5 (2018): 1–28, https://doi.org/10.1002/admi.201800074.
- 9. C. De Nardi, D. Gardner, D. Cristofori, L. Ronchin, A. Vavasori, and A. D. Jefferson, "Advanced 3D Printed Mini-Vascular Network for Self-Healing Concrete," *Materials & Design* 230 (2023): 111939.
- 10. Y. Shields, D. di Summa, N. Ospitia, et al., "A Large-Scale Demonstration and Sustainability Evaluation of Ductile-Porous Vascular Networks for Self-Healing Concrete," *Journal of Building Engineering* 95 (2024): 110040, https://doi.org/10.1016/j.jobe.2024.110040.
- 11. A. D. Jefferson and B. L. Freeman, "A Crack-Opening-dependent Numerical Model for Self-Healing Cementitious Materials," *International Journal of Solids and Structure* 244-245 (2022): 111601, https://doi.org/10.1016/j.ijsolstr.2022.111601.
- 12. B. L. Freeman and A. D. Jefferson, "A 3D Coupled Finite-Element Model for Simulating Mechanical Regain in Self-Healing Cementitious Materials," *ASCE Journal of Engineering Mechanics* 149, no. 7 (2023): 04023038, https://doi/10.1061/JENMDT.EMENG-6944.
- 13. A. Akhavan, S. M. H. Shafaatian, and F. Rajabipour, "Quantifying the Effects of Crack Width, Tortuosity, and Roughness on Water Permeability of Cracked Mortars," *Cement and Concrete Research* 42 (2012): 313–320, https://doi.org/10.1016/j.cemconres.2011.10.002.
- 14. N. Huang, R. Liu, and Y. Jiang, "Numerical Study of the Geometrical and Hydraulic Characteristics of 3D Self-Affine Rough Fractures During Shear," *Journal of Natural Gas Science and Engineering* 45 (2017): 127–142, https://doi.org/10.1016/j.jngse.2017.05.018.
- 15. Y. Zhang and J. Chai, "Effect of Surface Morphology on Fluid Flow in Rough Fractures: A Review," *Journal of Natural Gas Science and Engineering* 79 (2020): 103343, https://doi.org/10.1016/j.jngse.2020.103343.
- 16. E. Guiltinan, J. E. Santos, P. Purswani, and J. D. Hyman, "pySimFrac: A Python Library for Synthetic Fracture Generation and Analysis,"

- Computers and Geosciences 191 (2024): 105665, https://doi.org/10.1016/j. cageo.2024.105665.
- 17. N. Garcia and E. Stoll, "Monte Carlo Calculation for Electromagnetic-Wave Scattering From Random Rough Surfaces," *Physical Review Letters* 52, no. 20 (1984): 1798–1801, https://doi.org/10.1103/PhysRevLett.52.1798.
- 18. S. R. Brown, "Simple Mathematical Model of a Rough Fracture," *Journal of Geophysical Research* 100, no. B4 (1995): 5941–5952, https://doi.org/10.1029/94JB03262.
- 19. P. Glover, K. Matsuki, R. Hikima, and K. Hayashi, "Synthetic Rough Fractures in Rocks," *Journal of Geophysical Research: Solid Earth* 103, no. 5 (1998): 9609–9620, https://doi.org/10.1029/97JB02836.
- 20. S. R. Ogilvie, E. Isakov, and P. Glover, "Fluid Flow Through Rough Fractures in Rocks II: A New Matching Model for Rough Rock Fractures," *Earth and Planetary Science Letters* 241, no. 3-4 (2006): 454–465, https://doi.org/10.1016/j.epsl.2005.11.041.
- 21. J. E. Santos, A. Gigliotti, A. Bihanni, et al., "MPLBM-UT: Multiphase LBM Library for Permeable Media Analysis," *SoftwareX* 18 (2022): 101097, https://doi.org/10.1016/j.softx.2022.101097.
- 22. Y. Chen, A. J. Valocchi, Q. Kang, and H. S. Viswanathan, "Intertial Effects During the Process of Supercritical CO2 Displacing Brine in Sandstone: Lattice Boltzmann Simulations Based on the Continuum-Surface-Force and Geometrical Wetting Models," *Water Resources Research* 55, no. 12 (2019): 11144–11165, https://doi.org/10.1029/2019WR025746.
- 23. J. Arregui-Mena, L. Margetts, and P. M. Mummery, "Practical Applications of the Stochastic Finite Element Method," *Archives of Computational Methods in Engineering* 23 (2016): 171–190, https://doi.org/10.1007/s11831-014-9139-3.
- 24. G. A. Fenton and E. H. Vanmarcke, "Simulation of Random Fields via Local Average Subdivision," *Journal of Engineering Mechanics* 116, no. 8 (1990): 1733–1749, https://doi.org/10.1061/(asce)0733-9399(1990) 116:8(1733).
- 25. S. Montoya-Noguera, T. Zhao, Y. Hu, Y. Wang, and K. K. Phoon, "Simulation of Non-Stationary Non-Gaussian Random Fields From Sparse Measurements Using Bayesian Compressive Sampling and Karhunen-Loève Expansion," *Structural Safety* 79 (2019): 66–79, https://doi.org/10.1016/j.strusafe.2019.03.006.
- 26. A. M. J. Olsson and G. E. Sandberg, "Latin Hypercube Sampling for Stochastic Finite Element Analysis," *Journal of Engineering Mechanics* 128, no. 1 (2002): 121–125, https://doi.org/10.1061/(asce)0733-9399(2002) 128:1(121).
- 27. J. Shui-Hua, H. Jinsong, H. Faming, Y. Jianhua, Y. Chi, and Z. Chuang-Bing, "Modelling of Spatial Variability of Soil Undrained Shear Strength by Conditional Random Fields for Slope Reliability Analysis," *Applied Mathematical Modelling* 63 (2018): 374–389.
- 28. K. Tang, J. Wang, and L. Li, "A Prediction Method Based on Monte Carlo Simulations for Finite Element Analysis of Soil Medium Considering Spatial Variability in Soil Parameters," *Advances in Materials Science and Engineering* 2020 (2020): 7064640, https://doi.org/10.1155/2020/7064640.
- 29. L. Roininen, J. M. J. Huttunen, and S. Lasanen, "Whittle-Matérn Priors for Bayesian Statistical Inversion With Applications in Electrical Impedance Tomography," *Inverse Problems & Imaging* 8, no. 2 (2014): 561–586, https://doi.org/10.3934/ipi.2014.8.561.
- 30. E. A. B. F. Lima, D. Faghihi, R. Philley, et al., "Bayesian Calibration of a Stochastic, Multiscale Agent-Based Model for Predicting In Vitro Tumor Growth," *PLoS Computational Biology* 17, no. 11 (2021): e1008845, https://doi.org/10.1371/journal.pcbi.1008845.
- 31. F. Beckers, A. Heredia, M. Noack, W. Nowak, S. Wieprecht, and S. Oladyshkin, "Bayesian Calibration and Validation of a Large-Scale and Time-Demanding Sediment Transport Model," *Water Resources Research* 56 (2020): 026966, https://doi.org/10.1029/2019WR026966.
- 32. P. R. Wagner, R. Fahrni, M. Klippel, A. Frangi, and B. Sudret, "Bayesian Calibration and Sensitivity Analysis of Heat Transfer Models

- for Fire Insulation Panels," *Engineering Structures* 205 (2020): 110063, https://doi.org/10.1016/j.engstruct.2019.110063.
- 33. M. C. Kennedy and A. O'Hagan, "Bayesian Calibration of Computer Models," *Journal of the Royal Statistical Society Series B* 63, no. 3 (2001): 425–464, https://doi.org/10.1111/1467-9868.00294.
- 34. W. K. Liu, T. Belytschko, and A. Mani, "Random Field Finite Elements," *International Journal for Numerical Methods in Engineering* 23, no. 10 (1986): 1831–1845, https://doi.org/10.1002/nme.1620231004.
- 35. Ł. Figiel and M. Kamiński, "Numerical Probabilistic Approach to Sensitivity Analysis in a Fatigue Delamination Problem of a Two Layer Composite," *Applied Mathematics and Computation* 209 (2009): 75–90, https://doi.org/10.1016/j.amc.2008.06.039.
- 36. C. Soize, "Tensor-Valued Random Fields for Meso-Scale Stochastic Model of Anisotropic Elastic Microstructure and Probabilistic Analysis of Representative Volume Element Size," *Probabilistic Engineering Mechanics* 23 (2008): 307–323, https://doi.org/10.1016/j.probengmech. 2007.12.019.
- 37. M. Ostoja-Starzewski, "Microstructural Disorder, Mesoscale Finite Elements and Macroscopic Response," *Proceedings of the Royal Society A: Mathematical, Physical and Engineering Sciences* 455 (1999): 3189–3199, https://doi.org/10.1098/rspa.1999.0446.
- 38. E. J. Ricketts, B. L. Freeman, P. J. Cleall, A. D. Jefferson, and P. Kerfriden, "A Statistical Finite Element Method Integrating a Plurigaussian Random Field Generator for Multi-Scale Modelling of Solute Transport in Concrete," *Transport in Porous Media* 148, no. 1 (2023): 95–121, https://doi.org/10.1007/s11242-023-01930-8.
- 39. E. J. Ricketts, P. J. Cleall, A. D. Jefferson, P. Kerfriden, and P. Lyons, "Representation of Three-Dimensional Unsaturated Flow in Heterogeneous Soil Through Tractable Gaussian Random Field," *Geotechnique* 74 (2024): 1868–1880, https://doi.org/10.1680/jgeot.22.00316.
- 40. G. Stefanou, "The Stochastic Finite Element Method: Past, Present and Future," *Computer Methods in Applied Mechanics and Engineering* 198 (2009): 1031–1051, https://doi.org/10.1016/j.cma.2008.11.007.
- 41. T. D. Hien and M. Kleiber, "Stochastic Finite Element Modelling in Linear Transient Heat Transfer," *Computer Methods in Applied Mechanics and Engineering* 144 (1997): 111–124, https://doi.org/10.1016/S0045-7825(96)01168-1.
- 42. R. G. Ghanem and R. M. Kruger, "Numerical Solution of Spectral Stochastic Finite Element Systems," *Computer Methods in Applied Mechanics and Engineering* 129 (1996): 289–303, https://doi.org/10.1016/0045-7825(95)00909-4.
- 43. A. Poot, P. Kerfriden, I. Rocha, and F. van der Meer, "A Bayesian Approach to Modeling Finite Element Discretization Error," *Statistics and Computing* 34 (2024): 167, https://doi.org/10.1007/s11222-024-10463-z.
- 44. M. Girolami, E. Febrianto, G. Yin, and F. Cirak, "The Statistical Finite Element Method (statFEM) for Coherent Synthesis of Observation Data and Model Predictions," *Computer Methods in Applied Mechanics and Engineering* 375 (2021): 113533, https://doi.org/10.1016/j.cma.2020.113533.
- 45. Z. Dou, Z. Zhou, and B. E. Sleep, "Influence of Wettability on Interfacial Area During Immiscible Liquid Invasion Into a 3D Self-affine Rough Fracture: Lattice Boltzmann Simulations," *Advances in Water Resources* 61 (2013): 1–11, https://doi.org/10.1016/j.advwatres.2013.08.
- 46. E. J. Guiltinan, J. E. Santos, M. B. Cardenas, D. N. Espinoza, and Q. Kang, "Two-Phase Fluid Flow Properties of Rough Fractures With Heterogeneous Wettability: Analysis With Lattice Boltzmann Simulations," *Water Resources Research* 56 (2020): 027943.
- 47. Y. Dai, Z. Zhou, J. Lin, and J. Han, "Modeling of Two-Phase Flow in Rough-Walled Fracture Using Level Set Method," *Geofluids* (2017): 2429796.
- 48. Y. F. Chen, N. Guo, D. S. Wu, and R. Hu, "Numerical Investigation on Immiscible Displacement in 3D Rough Fracture: Comparison With Experiments and the Role of Viscous and Capillary Forces," *Advances*

- in Water Resources 118 (2018): 39–48, https://doi.org/10.1016/j.advwatres. 2018 05 016
- 49. S. Claus and P. Kerfriden, "A CutFEM Method for Two-Phase Flow Problems," *Computer Methods in Applied Mechanics and Engineering* 348 (2019): 185–206, https://doi.org/10.1016/j.cma.2019.01.009.
- 50. A. Lozinski, "CutFEM Without Cutting the Mesh Cells: A New Way to Impose Dirichlet and Neumann Boundary Conditions on Unfitted Meshes," *Computer Methods in Applied Mechanics and Engineering* 356 (2019): 75–100, https://doi.org/10.1016/j.cma.2019.07.008.
- 51. N. M. Atallah, C. Canuto, and G. Scovazzi, "The Second-Generation Shifted Boundary Method and Its Numerical Analysis," *Computer Methods in Applied Mechanics and Engineering* 372 (2020): 113341, https://doi.org/10.1016/j.cma.2020.113341.
- 52. K. Li, N. M. Atallah, G. A. Main, and G. Scovazzi, "The Shifted Interface Method: A Flexible Approach to Embedded Interface Computations," *International Journal for Numerical Methods in Engineering* 121, no. 3 (2020): 492–518, https://doi.org/10.1002/nme.6231.
- 53. S. Pande, P. Papadopoulos, and I. Babuška, "A Cut-Cell Finite Element Method for Poisson's Equation on Arbitrary Planar Domains," *Computer Methods in Applied Mechanics and Engineering* 383 (2021): 113875, https://doi.org/10.1016/j.cma.2021.113875.
- 54. B. L. Freeman and A. D. Jefferson, "The Simulation of Transport Processes in Cementitious Materials With Embedded Healing Systems," *International Journal for Numerical and Analytical Methods in Geomechanics* 44 (2020): 293–326, https://doi.org/10.1002/nag.3017.
- 55. A. R. Khoei and S. Saeedmonir, "Computational Homogenization of Fully Coupled Multiphase Flow in Deformable Porous media," *Computer Methods in Applied Mechanics and Engineering* 376 (2021): 113660, https://doi.org/10.1016/j.cma.2020.113660.
- 56. A. R. Khoei, S. Saeedmonir, N. Hosseini, and S. M. Mousavi, "An X-FEM Technique for Numerical Simulation of Variable-Density Flow in Fractured Porous Media," *MethodsX* 10 (2023): 102137, https://doi.org/10.1016/j.mex.2023.102137.
- 57. T. Mohammadnejad and A. R. Khoei, "Hydro-Mechanical Modeling of Cohesive Crack Propagation in Multiphase Porous Media Using the Extended Finite Element Method," *International Journal for Numerical and Analytical Methods in Geomechanics* 37 (2013): 1247–1279, https://doi.org/10.1002/nag.2079.
- 58. J. Réthoré, R. de Borst, and M. Abellan, "A Two-Scale Model for Fluid Flow in an Unsaturated Porous Medium With Cohesive Cracks," *Computational Mechanics* 42 (2008): 227–238.
- 59. T. S. Jiang, O. H. Soo-Gun, and J. C. Slattery, "Correlation for Dynamic Contact Angle," *Journal of Colloid & Interface Science* 69 (1979): 74–77, https://doi.org/10.1016/0021-9797(79)90081-X.
- 60. T. Belem, F. Homand-Etienne, and M. Souley, "Quantitative Parameters for Rock Joint Surface Roughness," *Rock Mechanics and Rock Engineering* 33, no. 4 (2000): 217–242, https://doi.org/10.1007/s006030070001.
- 61. E. J. Ricketts, P. J. Cleall, A. D. Jefferson, P. Kerfriden, and P. Lyons, "The Influence of Spatially Varying Boundary Conditions Based on Material Heterogeneity," *European Journal of Computational Mechanics* (2024): 199–226, https://doi.org/10.13052/ejcm2642-2085.3331.
- 62. F. Lindgren, H. Rue, and J. Lindström, "An Explicit Link Between Gaussian Fields and Gaussian Markov Random Fields: The Stochastic Partial Differential Equation Approach," *Journal of the Royal Statistical Society: Series B (Statistical Methodology)* 73, no. 4 (2011): 423–498, https://doi.org/10.1111/j.1467-9868.2011.00777.x.
- 63. C. E. Rasmussen and C. K. I. Williams, Gaussian Processes for Machine Learning (MIT Press, 2008).
- 64. P. D. Spanos and R. Ghanem, "Stochastic Finite Element Expansion for Random media," *Journal of Engineering Mechanics* 115, no. 5 (1989): 1035–1053, https://doi.org/10.1061/(ASCE)0733-9399(1989)115:5(1035).
- 65. A. Hansbo and P. Hansbo, "An Unfitted Finite Element Method, Based on Nitsche's Method, for Elliptic Interface Problems," *Computer Methods*

- in Applied Mechanics and Engineering 191 (2002): 5537–5552, https://doi.org/10.1016/S0045-7825(02)00524-8.
- 66. B. L. Freeman, "A Multi-Point Constraint Unfitted Finite Element Method," *Advanced Modeling and Simulation in Engineering Sciences* 9 (2022): 19, https://doi.org/10.1186/s40323-022-00232-w.
- 67. H. M. Mourad, J. Dolbow, and K. Garikipati, "An Assumed-Gradient Finite Element Method for the Level Set Equation," *International Journal for Numerical Methods in Engineering* 64 (2005): 1009–1032, https://doi.org/10.1002/nme.1395.
- 68. S. Groß, V. Reichelt, and A. Reusken, "A Finite Element Based Level Set Method for Two-phase Incompressible Flows," *Computer Vision Science* 9 (2006): 239–257, https://doi.org/10.1007/s00791-006-0024-y.
- 69. E. J. Ricketts, P. J. Cleall, A. D. Jefferson, P. Kerfriden, and P. Lyons, "Near-Boundary Error Reduction With an Optimized Weighted Dirichlet-Neumann Boundary Condition for Stochastic PDE-Based Gaussian Random Field Generators," *Engineering With Computers* 39, no. 6 (2023b): 3821–3833, https://doi.org/10.1007/s00366-023-01819-6.
- 70. C. Sherlock, P. Fearnhead, and G. O. Roberts, "The Random Walk Metropolis: Linking Theory and Practice Through a Case Study," *Statistical Science* 25, no. 2 (2010): 172–190, https://doi.org/10.1214/10-STS327.
- 71. S. P. Brooks and A. Gelman, "General Methods for Monitoring Convergence of Iterative Simulations," *Journal of Computational and Graphical Statistics* 7, no. 4 (1998): 434–455, https://doi.org/10.1080/10618600.1998. 10474787.
- 72. F. James and L. Moneta, "Review of High-Quality Random Number Generators," *Computing and Software for Big Science* 4 (2020): 2, https://doi.org/10.1007/s41781-019-0034-3.
- 73. L. Crocetti, P. Nannipieri, S. Di Matteo, L. Fanucci, and S. Saponara, "Review of Methodologies and Metrics for Assessing the Quality of Random Number Generators," *Electronics* 12 (2023): 723, https://doi.org/10.3390/electronics12030723.
- 74. J. L. Crespo, J. González-Villa, J. Gutiérrez, and A. Valle, "Assessing the Quality of Random Number Generators Through Neural Networks," *Machine Learning Science and Technology* 5 (2024): 025072, https://doi.org/10.1088/2632-2153/ad56fb.
- 75. P. Yin, C. Zhao, J. Ma, C. Yan, and L. Huang, "Experimental Study of Non-Linear Fluid Flow Through Rough Fracture Based on Fractal Theory and 3D Printing Technique," *International Journal of Rock Mechanics and Mining Sciences* 129 (2020): 104293, https://doi.org/10.1016/j.ijrmms.2020. 104293.
- 76. N. O. Myers, "Characterization of Surface Roughness," *Precision Engineering* 3, no. 2 (1962): 97–104.
- 77. D. Li and S. Liu, "Macro Polypropylene Fiber Influences on Crack Geometry and Water Permeability of Concrete," *Construction and Building Materials* 231 (2020): 117128, https://doi.org/10.1016/j.conbuildmat. 2019.117128.
- 78. C. Wu, J. Chu, S. Wu, and Y. Hong, "3D Characterization of Microbially Induced Carbonate Precipitation in Rock Fracture and the Resulted Permeability Reduction," *Engineering Geology* 249 (2019): 23–30, https://doi.org/10.1016/j.enggeo.2018.12.017.
- 79. D. Gardner, A. D. Jefferson, and A. Hoffman, "Investigation of Capillary Flow in Discrete Cracks in Cementitious Materials," *Cement and Concrete Research* 42 (2012): 972–981, https://doi.org/10.1016/j.cemconres. 2012.03.017.
- 80. D. Gardner, A. D. Jefferson, A. Hoffman, and R. Lark, "Simulation of the Capillary Flow of an Autonomic Healing Agent in Discrete Cracks in Cementitious Materials," *Cement and Concrete Research* 58 (2014): 35–44, https://doi.org/10.1016/j.cemconres.2014.01.005.
- 81. G. O. Roberts, A. Gelman, and W. R. Gilks, "Weak Convergence and Optimal Scaling of Random Walk Metropolis Algorithms," *The Annals of Applied Probability* 7, no. 1 (1997): 110–120.

82. W. A. Link and M. J. Eaton, "On Thinning of Chains in MCMC," *Methods in Ecology and Evolution* 3 (2012): 112–115, https://doi.org/10.1111/j.2041-210X.2011.00131.x.

83. J. Zhu, R. Zhang, Y. Zhang, and F. He, "The Fractal Characteristics of Pore Size Distribution in Cement-Based Materials and Its Effect on Gas Permeability," *Scientific Reports* 9 (2019): 17191, https://doi.org/10.1038/s41598-019-53828-5.

84. D. Gardner, D. Herbert, M. Jayaprakash, A. D. Jefferson, and A. Paul, "Capillary Flow Characteristics of an Autogenic and Autonomic Healing Agent for Self-Healing Concrete," *Journal of Materials in Civil Engineering* 29 (2017): 04017228, https://doi.org/10.1061/(ASCE)MT.1943-5533.0002092.

85. B. Iglewicz and D. C. Hoaglin, *Volume 16: How to Detect and Handle Outliers* (Quality Press, 1993).

## Appendix A: Determination of Statistical Parameters of Crack Asperities and Crack Width Variation

When generating a field in the model, we must supply a correlation length to determine the correlation structure, and a mean value and standard deviation by which the field will be scaled.

To this end, images of crack profiles were taken from the experimental samples. The images were taken using a DSLR camera whilst lighting the sample against a black backdrop, clearly highlighting the crack profile along the edges of the sample. An image analysis script was then written in Python to determine the relative height of asperities. Figure A1 shows the raw image and its transformation due to suitable thresholding and morphological transformations. Once the relative heights of the asperities were attained, a variogram was calculated based on the data to estimate the correlation length of the crack. The mean value and standard deviation of the heights were also computed based on the measured profile, ready for model input to scale the random field realisations. In order to determine the fractal dimension, as well as the constants found in the fractal relationships (Equations 11 and 12), the calculation was repeated for different measurement lengths (or length-scales).

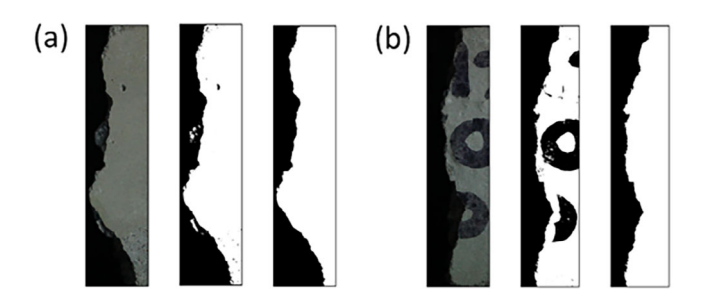


**FIGURE A1** | Image processing for two faces of the fracture sample. From left to right in both (a) and (b), we have the raw image, threshold image and after the applying morphological operations.

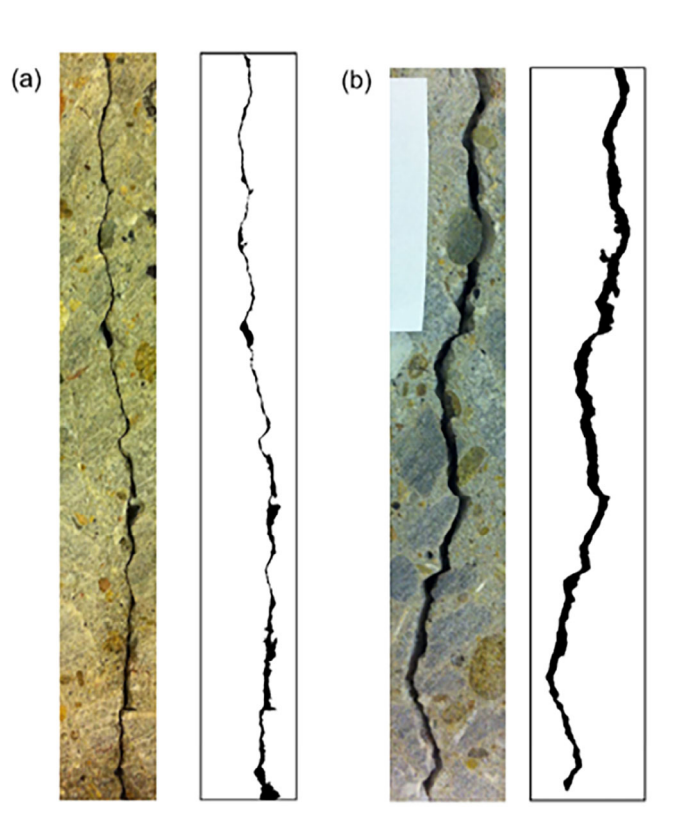


**FIGURE A2** | Image processing for the determination of crack width variation, where (a) is the water sample and (b) is the ground-granulated blast furnace slag (GGBS) sample.

The final term to be determined was the variation in crack width, as represented in the model by smoothed Gaussian noise. The image processing was conducted similarly to the above, where the crack was isolated from its associated image (see Figure A2).

From this, the crack width was evaluated based on pixel density for each row of pixels, where the mean and standard deviation could then be established. These were then used to scale the smoothed noise that represents the crack width. It is assumed in both cases that the crack profiles along the edge are representative of the topography across the full crack interfaces.

#### Appendix B: Random Realisations of Concrete Cracks

The mean asperity height employed in the simulations was 10 mm, and as noted in Section 4, it is the relative asperity heights that determine the fluid flow properties rather than the absolute value. The random realisations of crack asperities can be seen in Figure B1, whilst the calculated roughness and tortuosity can be seen in Figures B2 and B3. Finally, the smoothed Gaussian noise representation of the crack width variation due to material loss for each of the realisations can be seen in Figure B4.

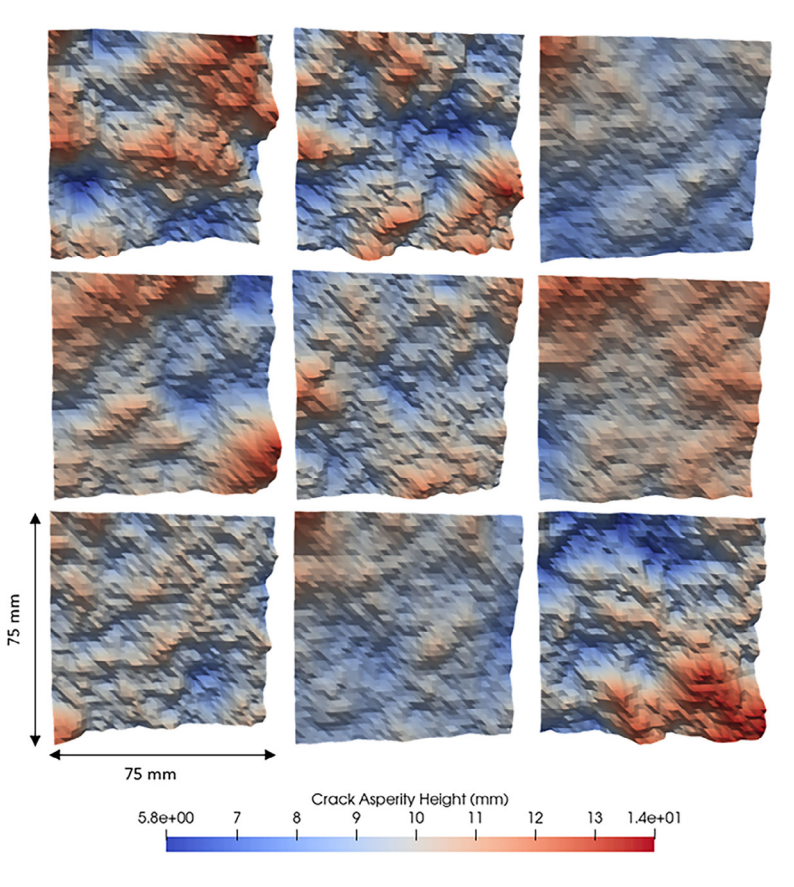
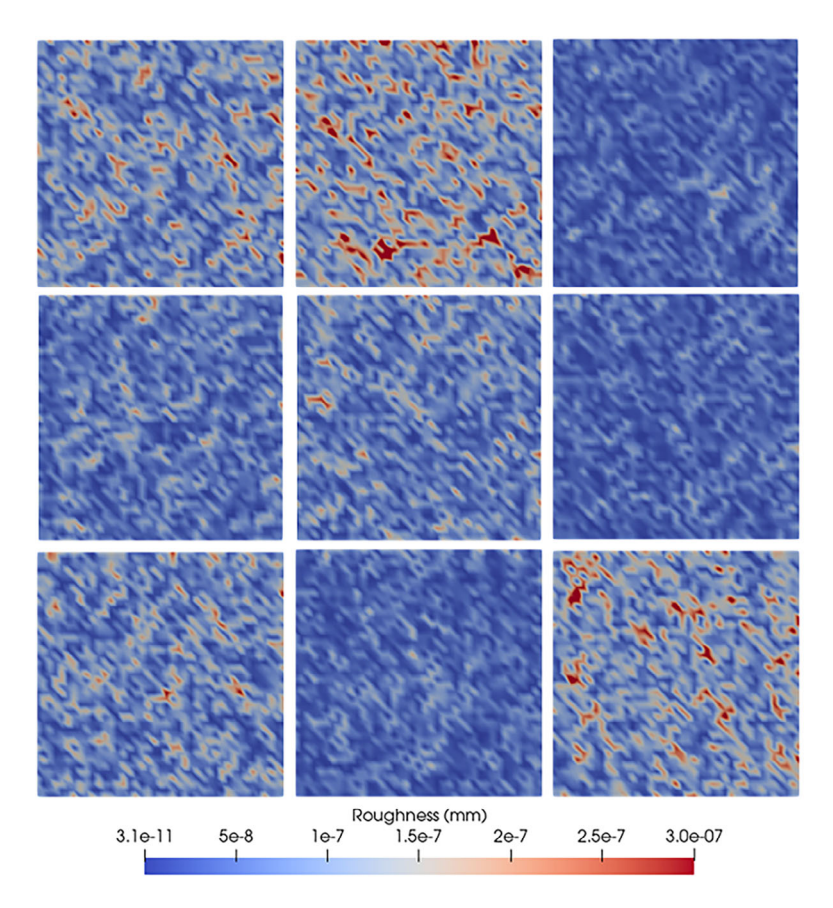
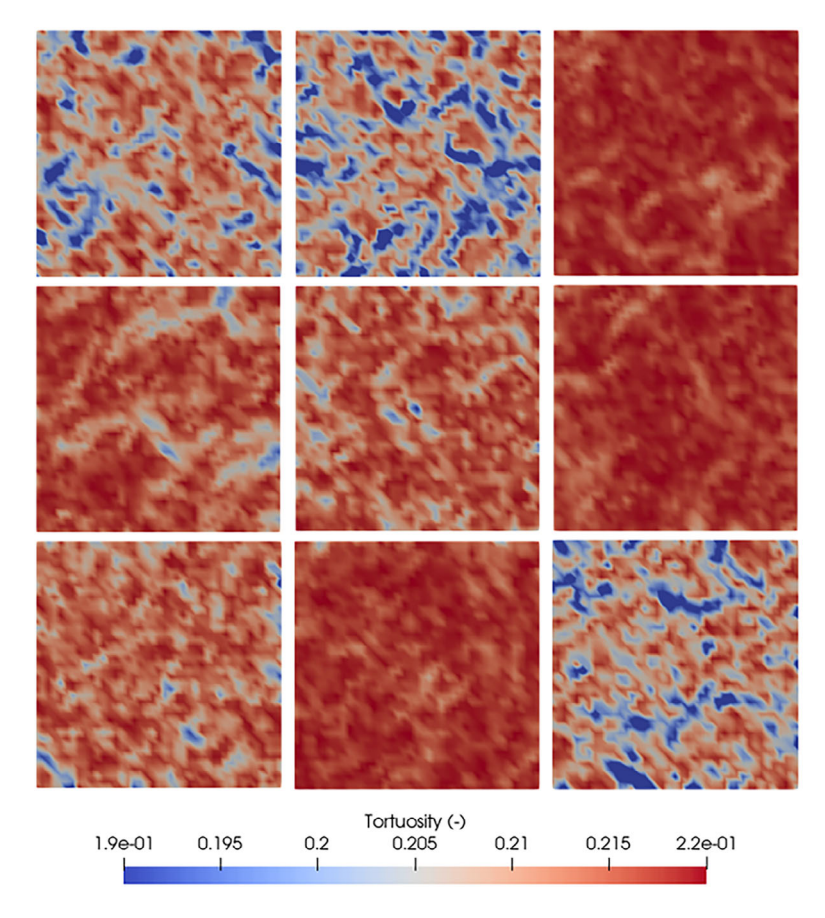


FIGURE B1 | Crack asperities for Realisations 1–9 shown left to right, top to bottom.



 $\textbf{FIGURE} \quad \textbf{B2} \quad | \quad \text{Calculated roughness for Realisations 1-9 shown left to right, top to bottom.}$ 



**FIGURE B3** Calculated tortuosity for Realisations 1–9 shown left to right, top to bottom.

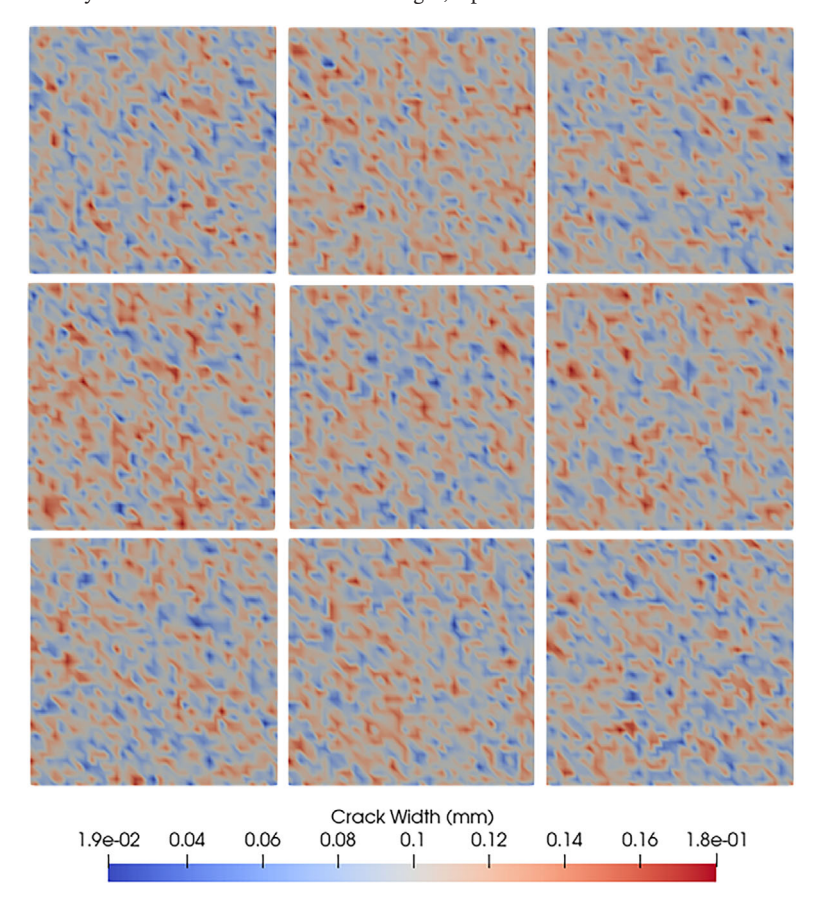


**FIGURE B4** | Spatially varying crack widths for Realisations 1–9 shown left to right, top to bottom.